AD-A041 520   UNITED TECHNOLOGIES RESEARCH CENTER EAST HARTFORD CONN   F/G 20/5
INVESTIGATION OF PLASMA PROCESSES IN ELECTRONIC TRANSITION LASE--ETC(U)
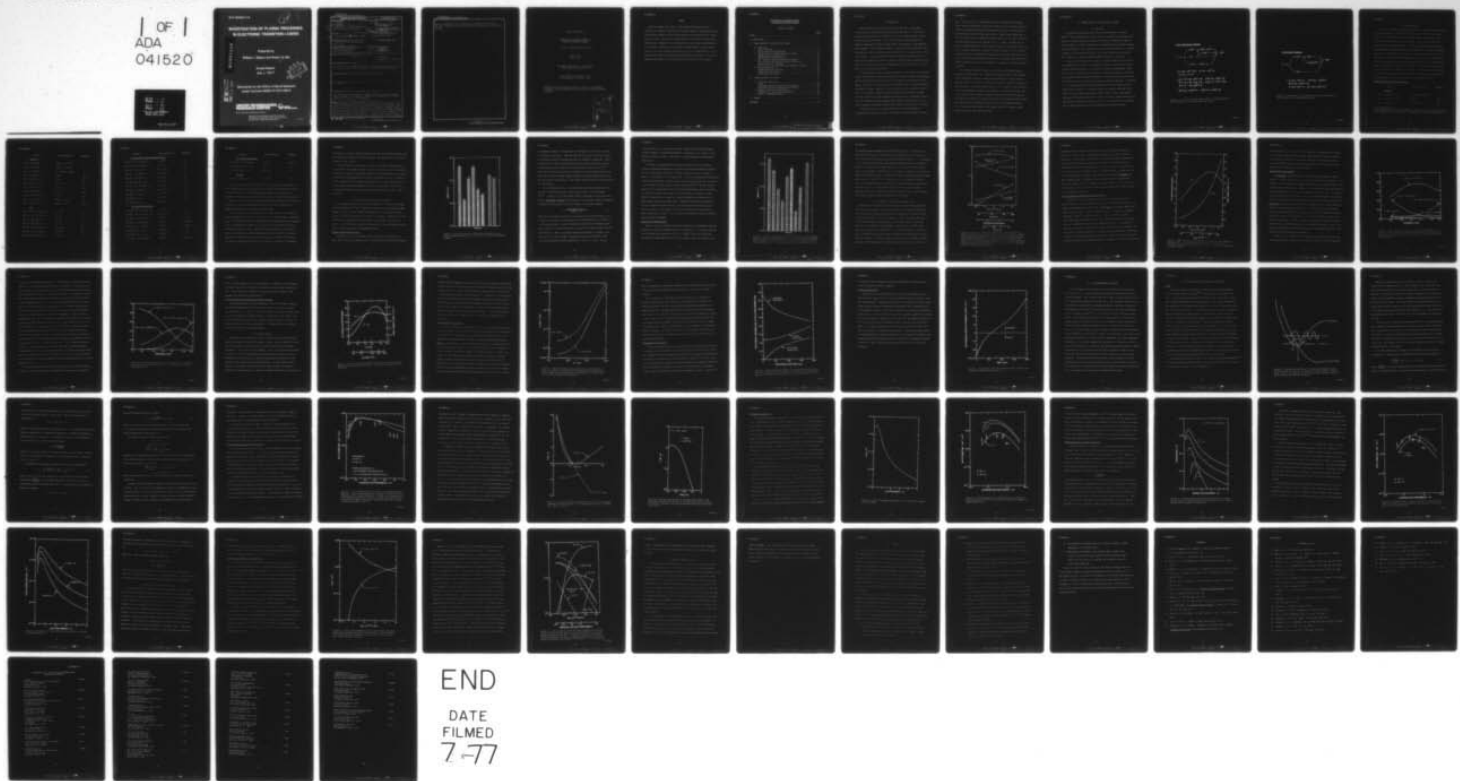JUL 77   W L NIGHAN , R J HALL   N00014-76-C-0847
UNCLASSIFIED   UTRC-R77-922617-2   NL

| OF |
ADA
041520

END
DATE
FILMED
7-77

R77-922617-2

ADA041520

INVESTIGATION OF PLASMA PROCESSES IN ELECTRONIC TRANSITION LASERS

Prepared by

William L. Nighan and Robert J. Hall

Annual Report

July 1, 1977

DDC
JUL 12 1977

Sponsored by the Office of Naval Research

Under Contract N00014-76-C-0847

AD No. ___ DDC FILE COPY

UNITED TECHNOLOGIES RESEARCH CENTER

UNITED TECHNOLOGIES™

EAST HARTFORD, CONNECTICUT 06108

77—06—221—1

REPORT DOCUMENTATION PAGE		READ INSTRUCTIONS BEFORE COMPLETING FORM
1. REPORT NUMBER R77-922617-2	2. GOVT ACCESSION NO.	3. RECIPIENT'S CATALOG NUMBER
4. TITLE *(and Subtitle)* Investigation of Plasma Processes in Electronic Transition Lasers		5. TYPE OF REPORT & PERIOD COVERED Annual Report, June 1, 1976–July 1, 1977
		6. PERFORMING ORG. REPORT NUMBER R77-922617-2
7. AUTHOR(s) William L. Nighan and Robert J. Hall		8. CONTRACT OR GRANT NUMBER(s) N00014-76-C-0847
9. PERFORMING ORGANIZATION NAME AND ADDRESS United Technologies Research Center Silver Lane East Hartford, CT 06108		10. PROGRAM ELEMENT, PROJECT, TASK AREA & WORK UNIT NUMBERS
11. CONTROLLING OFFICE NAME AND ADDRESS Office of Naval Research Physics Program Office 800 N. Quincy Street, Arlington, VA 22717		12. REPORT DATE July 1, 1977
		13. NUMBER OF PAGES 62
14. MONITORING AGENCY NAME & ADDRESS *(if different from Controlling Office)*		15. SECURITY CLASS. *(of this report)* Unclassified
		15a. DECLASSIFICATION DOWNGRADING SCHEDULE

16. DISTRIBUTION STATEMENT *(of this Report)*

Approved for public release; distribution unlimited. Reproduction in whole
or in part is permitted for any purpose of the United States Government.

17. DISTRIBUTION STATEMENT *(of the abstract entered in Block 20, if different from Report)*

18. SUPPLEMENTARY NOTES

19. KEY WORDS *(Continue on reverse side if necessary and identify by block number)*

Rare gas-halide laser kinetics, KrF lasers, electronic transition lasers,
plasma processes in KrF lasers, F_2 dissociative attachment, F_2 vibrational
excitation, F_2 dissociation by electrons.

20. ABSTRACT *(Continue on reverse side if necessary and identify by block number)*

Plasma processes in electrically excited rare gas-halide lasers have been
investigated theoretically, with particular emphasis on the KrF system. These
studies have resulted in the identification of fundamental processes influen-
cing electron energy transfer, charged particle production and loss, metastable
production and loss, and plasma stability. Both electron beam pumped and dis-
charge pumped lasers have been examined. In addition, resonance scattering
theory has been applied to available e-F_2 attachment data in order to determine

DD FORM 1473 EDITION OF 1 NOV 65 IS OBSOLETE

20.

electron cross-sections for F_2 dissociative attachment and vibrational excitation. Estimates of direct electron impact dissociation of F_2 have also been made.

Report R77-922617-2

INVESTIGATION OF PLASMA PROCESSES IN
ELECTRONIC TRANSITION LASERS

William L. Nighan and Robert J. Hall

Annual Report
July 1, 1977

PREFACE

Under the present ONR Contract, United Technologies Research Center is conducting an analytical investigation of plasma processes in electrically excited rare gas-halide lasers, with particular emphasis directed toward the KrF^* system. This work is being carried out in coordination with a Corporate sponsored experimental program. Emphasis in this investigation is being placed on identification of fundamental processes influencing electron energy transfer, charged particle production and loss, metastable production and loss, and plasma stability. Both electron-beam pumped and discharge pumped systems are being studied. This report summarizes the results of the activity under the first year of the contract.

R77-922617-2

Investigation of Plasma Processes
in Electronic Transition Lasers

TABLE OF CONTENTS

iii

I. INTRODUCTION

During the past year significant progress has been made in experimental investigations of electrically excited rare gas-halide lasers.[1] In particular, electrical-optical conversion efficiencies in the 1-10% range have been reported for the KrF^* and XeF^* systems. Prior to the discovery of these lasers there existed no experience with high pressure highly ionized/excited, volume dominated glow discharges. Thus, although progress in this area has been surprisingly rapid, understanding of basic processes in these discharges is in a relatively early stage of development. Since rare gas-halide systems and similar candidates such as the mercury halides offer the potential of scalable, efficient short wavelength lasers, evolution of significantly improved understanding of basic processes in the plasma medium is of considerable importance.

For these reasons, under the present ONR contract, United Technologies Research Center is conducting an analytical investigation of plasma processes in electrically excited rare gas-halide lasers, with particular emphasis directed toward the KrF^* system. This work is being carried out in coordination with a Corporate-sponsored experimental program. Emphasis in this investigation is being placed on identification of fundamental processes influencing electron energy transfer, charged particle production and loss, metastable production and loss, and plasma stability. Both electron-beam pumped and discharge pumped systems are being studied. This report summarizes the results of the activity under the first year of the contract.

Presented in Sec. II is a general description of the plasma modeling procedures being utilized along with a discussion of numerical results obtained to

1

date. In particular, it is shown that KrF^* can be produced with a discharge energy conversion efficiency on the order of 50%, and that the overall electrical-to-optical conversion efficiency could reach levels in the 10 to 20% range for both discharge pumped and e-beam pumped lasers. Values of small signal gain in the 0.5-1.5% cm^{-1} range are predicted for these conditions. The factors affecting discharge instability are also treated in Sec. II. There it is shown that in certain circumstances direct electron impact ionization of ground state atoms can have an important deleterious influence on plasma stability. Direct ionization becomes competitive with metastable ionization at high values of fractional ionization for which the number density of electrons in the high energy region of the electron distribution function is increased as a consequence of electron-electron collisions.

The potential influence of electron collisions with the halogen bearing molecule is treated in Sec. III. Therein is discussed the basis of an estimate of e-F_2 vibrational excitation cross-sections determined by fitting resonance scattering theory to available F_2 dissociative attachment rate data. Estimates of the cross-section for electron impact excitation of F_2 leading to direct dissociation are also discussed. Based on this analysis it is concluded that both vibrational excitation and electronic excitation of the halogen containing molecule are likely to be important for conditions typical of rare gas-halide laser plasmas. The principal results discussed in Secs. II and III are summarized briefly in Sec. IV along with those aspects of the research which are to receive primary emphasis during the last half of this year.
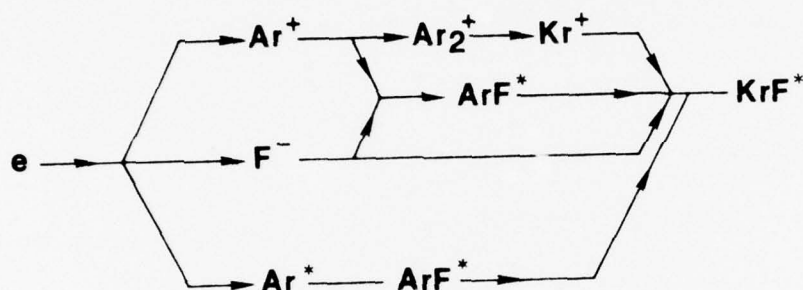
II. PLASMA KINETICS IN RARE GAS-HALIDE PLASMAS

A. Background

Rare gas-halide lasers have been pumped successfully both by electron-beams,[2,3] and by discharges; the latter externally sustained[4] and self-sustained.[5] However, the excimer production process is substantially different for these two pumping schemes. In order to qualitatively illustrate the more important features of excimer formation in high pressure rare gas halide lasers, Figs. 1 and 2 present illustrations of the general features of the primary reaction chains leading to KrF^* production in e-beam and discharge pumped mixture of Ar, Kr and F_2.

Figures 1 and 2 indicate that, unlike ir molecular lasers such as CO_2 and/or CO for example, KrF^* (or XeF^*) is produced by reactions proceeding along several parallel collision channels in both e-beam and discharge pumped systems. Examination of Fig. 1 shows that KrF^* production in e-beam pumped systems is dominated by three-body neutral stabilized recombination of positive and negative ions which are produced initially by high energy primary and secondary electrons. In contrast, in a controlled, externally sustained discharge, binary excited state reactions dominate KrF^* production. It should be pointed out, however, that under certain conditions, particularly those typical of high current density, self-sustained discharges,[5] KrF^* excimer production is likely to involve a complex combination of the reactions illustrated in both Figs. 1 and 2. In any case, KrF^* is ultimately lost by radiative decay and by two and three body collisional quenching.

ELECTRON BEAM PUMPING

$$e \longrightarrow \quad \begin{array}{c} Ar^+ \longrightarrow Ar_2^+ \longrightarrow Kr^+ \\ ArF^* \longrightarrow \\ F^- \\ Ar^* \longrightarrow ArF^* \longrightarrow \end{array} \longrightarrow KrF^*$$

- $e + Ar \longrightarrow Ar^+ + 2e$; $e + Ar \longrightarrow Ar^* + e$

  $e + F_2 \longrightarrow F + F^-$

- $Ar^+ + F^- + M \longrightarrow ArF^* + M$; $ArF^* + Kr \longrightarrow KrF^* + Ar$

  $Ar^+ + Ar + M \longrightarrow Ar_2^+ + M$; $Ar_2^+ + Kr \longrightarrow Kr^+ + 2Ar$

  $Kr^+ + F^- + M \longrightarrow KrF^* + M$

- $Ar^* + F_2 \longrightarrow ArF^* + F$; $ArF^* + Kr \longrightarrow KrF^* + Ar$

Figure 1. Illustration of the primary reaction processes leading to KrF* production in an electron-beam pumped laser.

4

DISCHARGE DUMPING

$$e \rightarrow \begin{array}{c} Ar^* \rightarrow ArF^* \\ Ar_2^* \rightarrow Kr^* \\ Kr^* \end{array} \rightarrow KrF^*$$

- $e + Ar \rightarrow Ar^* + e$; $Ar^* + F_2 \rightarrow ArF^* + F$

  $ArF^* + Kr \rightarrow KrF^* + Ar$

  $e + Kr \rightarrow Kr^* + e$; $Kr^* + F_2 \rightarrow KrF^* + F$
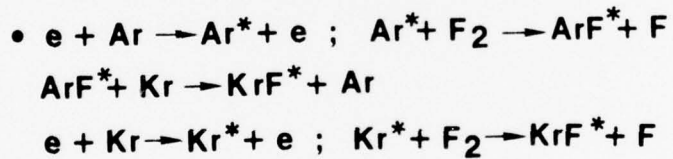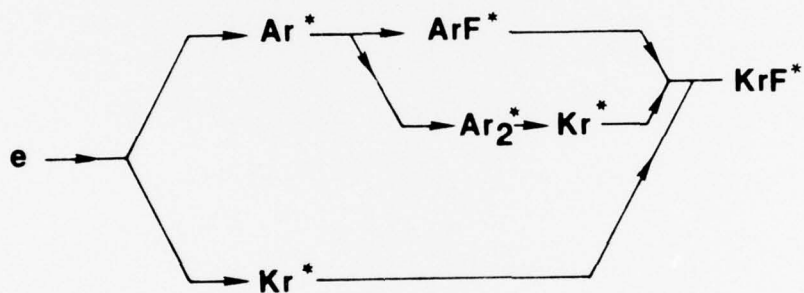
Figure 2. Illustration of the primary reaction processes leading to KrF* production in a discharge pumped laser.

77—06—84—7

5

B. Kinetic Modeling

In order to identify and understand the primary collisional reactions occurring in the high pressure ($\gtrsim 1$ atm), highly ionized ($n_e/n \sim 10^{-6}$-10^{-5}), and highly excited ($n^*/n \sim 10^{-5}$-10^{-4}) plasmas of interest, numerical models of the temporal evolution of the concentrations of ion species and excited species have been developed under the present contract. In this work, efforts have been directed toward generation of insight rather than on development of a totally comprehensive description of plasma behavior. Emphasis in the studies carried out to date has been placed on electrically excited mixtures of Ar, Kr and F_2. The mathematical features of the model are entirely straightforward and will not be elaborated upon. Rather, consideration of the reaction processes included permits a better appreciation of the important aspects of the analysis. The following table summarizes the primary time dependent reactions considered in this analysis, typical values of rate coefficients, and data sources other than present work (PW).

Table of Reactions and Rate Coefficients

Reaction	Rate Coefficient[*]	Reference
Electrons		
(1) $e_p + Ar \rightarrow Ar^+ + 2e$	ext. source, variable	--
(2) $e + Ar^* \rightarrow Ar^+ + 2e$	2×10^{-8}	PW, 9
(3) $e + F_2 \rightarrow F^- + F$	$f(E/n), \sim 10^{-9}$	PW, 6

[*]Rate coefficients for two-body processes are expressed in $\sec^{-1}$ cm^3 and for three-body processes in units of $\sec^{-1}$ cm^6. Radiative decay rates are expressed as $\sec^{-1}$.

Reaction	Rate Coefficient[*]	Reference
Electrons		
(4) $e + Ar_2^+ \rightarrow 2Ar$	$f(E/n), \sim 3 \times 10^{-8}$	7
(5) $e + Kr_2^+ \rightarrow 2Kr$	$f(E/n), \sim 5 \times 10^{-8}$	7
(6) $e_p + Ar \rightarrow Ar^* + e$	ext. source, variable	-
(7) $e + Ar \rightarrow Ar^* + e$	$f(E/n)$	PW, 8
(8) $e + Kr \rightarrow Kr^* + e$	$f(E/n)$	PW
(9) $e + Ar^* \rightarrow Ar + e$	3.8×10^{-9}	PW
(10) $e + Kr^* \rightarrow Kr + e$	3.8×10^{-9}	PW
(11) $e + Ar^* \rightarrow Ar^{**} + e$	2×10^{-7}	PW, 9
(12) $e + Kr^* \rightarrow Kr^{**} + e$	2×10^{-7}	PW
(13) $e + F_2 \rightarrow F_2(v) + e$	$f(E/n), 2.5 \times 10^{-9}$	PW
(14) $e + F_2 \rightarrow F + F + e$	$f(E/n), \sim 10^{-9}$	PW, 10
Ions		
(15) $F^- + Ar^+ + M \rightarrow ArF^* + M$	1×10^{-25}	7, 1
(16) $F^- + Kr^+ + M \rightarrow KrF^* + M$	1×10^{-25}	7, 1
(17) $F^- + Ar_2^+ \rightarrow ArF^* + Ar$	1×10^{-6}	7, 1
(18) $F^- + Kr_2^+ \rightarrow KrF^* + Kr$	1×10^{-6}	7, 1
(19) $Ar^+ + Ar + M \rightarrow Ar_2^+ + M$	2.3×10^{-31}	11
(20) $Kr^+ + Kr + M \rightarrow Kr_2^+ + M$	6×10^{-32}	12
(21) $Ar_2^+ + Kr \rightarrow Kr^+ + 2Ar$	3×10^{-10}	13

Reaction	Rate Coefficient*	Reference
Rare Gas Metastables and Excited Dimers		
(22) $Ar^* + Ar + M \rightarrow Ar_2^* + M$	1×10^{-32}	14
(23) $Kr^* + Kr + M \rightarrow Kr_2^* + M$	5×10^{-32}	14
(24) $Ar^* + F_2 \rightarrow ArF^* + F$	7.5×10^{-10}	15
(25) $Kr^* + F_2 \rightarrow KrF^* + F$	7.2×10^{-10}	15
(26) $Ar^* + Kr \rightarrow Kr^{**} + Ar$	6×10^{-12}	16
(27) $Ar_2^* + Kr \rightarrow Kr^* + 2Ar$	8×10^{-11}	14
(28) $Kr^* + Ar + M \rightarrow ArKr^* + M$	1×10^{-32}	14
(29) $Ar_2^* + F_2 \rightarrow Ar_2F^* + F$	2.5×10^{-10}	14
(30) $Kr_2^* + F_2 \rightarrow Kr_2F^* + F$	3×10^{-10}	14
(31) $Ar_2^* \rightarrow 2Ar + h\nu$	3.8×10^6	14
(32) $Kr_2^* \rightarrow 2Kr + h\nu$	3.3×10^6	14
Rare Gas-Halide Excimers		
(33) $ArF^* + Ar + M \rightarrow Ar_2F^* + M$	2×10^{-33}	14
(34) $KrF^* + Kr + M \rightarrow Kr_2F^* + M$	6.5×10^{-31}	17, 1
(35) $ArF^* + Kr \rightarrow KrF^* + Ar$	3×10^{-10}	1, 14
(36) $ArF^* + F_2 \rightarrow Products$	1×10^{-9}	1, 14, 15
(37) $KrF^* + F_2 \rightarrow Products$	1×10^{-9}	1, 14, 15
(38) $ArF^* \rightarrow Ar + F + h\nu$	3.3×10^7	14
(39) $KrF^* \rightarrow Kr + F + h\nu$	1.5×10^8	14
(40) $Ar_2F^* + F_2 \rightarrow Products$	1×10^{-9}	1, 14, 15

Reaction	Rate Coefficient[*]	Reference
Rare Gas-Halide Excimers		
(41) $Kr_2F^* + F_2 \rightarrow$ Products	1×10^{-9}	1, 14, 15
(42) $Ar_2F^* \rightarrow 2Ar + F + h\nu$	5×10^7	14
(43) $Kr_2F^* \rightarrow 2Kr + F + h\nu$	6.7×10^7	14
Fluorine		
(44) $F + F + M \rightarrow F_2 + M$	6×10^{-31}	18

In this table excited atoms denoted with a single asterisk represent the Ar and Kr metastable states (s states), while the double asterisk refers to Ar and Kr p states.[9] Electron rate coefficients were determined by averaging known (or estimated) cross-sections over electron energy distributions which were calculated as a function of gas mixture, E/n, metastable fractional concentration, and fractional ionization. For those processes for which the electron rate coefficient is an exceptionally strong function of E/n no value is given.

In many instances "best estimates" for rate coefficients for ion and excited state processes have evolved over the past year but at this date remain unpublished; while in other cases the same rate coefficient has been used for analogous processes in which a measured rate coefficient is available. In such situations the most appropriate reference is given. Because of such uncertainties in the values of certain rate coefficients, numerical experimentation was carried out by varying specific rate coefficients over rather wide ranges. Fortunately, KrF^* densities and production efficiencies were found to be relatively insensitive to reasonable

variations in rate data, reflecting the fact that the rare gas-halide excimer states are produced and destroyed by multiple collision processes with no single process dominating (Figs. 1 and 2).

Although there are uncertainties in the rate coefficients presented above, it is likely that the greatest jeopardy to quantitative analysis is due to the omission of important collisional reactions which have yet to be identified, such as electron collisions with the halogen-bearing molecule, for example (Sec. III). In addition, little is known about the absorption characteristics of various excited state and ionic species, although photodissociation of the rare gas dimer ions Ar_2^+, Kr_2^+..., is presently thought to be a very important absorption process for the uv laser radiation.[1]

C. Charged Particle and Excited State Densities

As a consequence of the relatively high pressures (~ 1 atm) and high charged particle densities ($\sim 10^{14}$ cm^{-3}) required to produce gain in rare gas-halide laser systems, the time to achieve essentially steady state conditions with constant pumping is found to be typically on the order of 10-30 nsec. Therefore, it is most informative to analyze plasma conditions after a quasi-steady state has been achieved. For this reason, the data to be discussed in this and subsequent sections refer to plasma properties in the quasi-steady regime.

Charged Particle Concentrations

Presented in Fig. 3 are computed electron, negative ion and positive ion densities for conditions representative of an electron-beam pumped KrF laser mixture
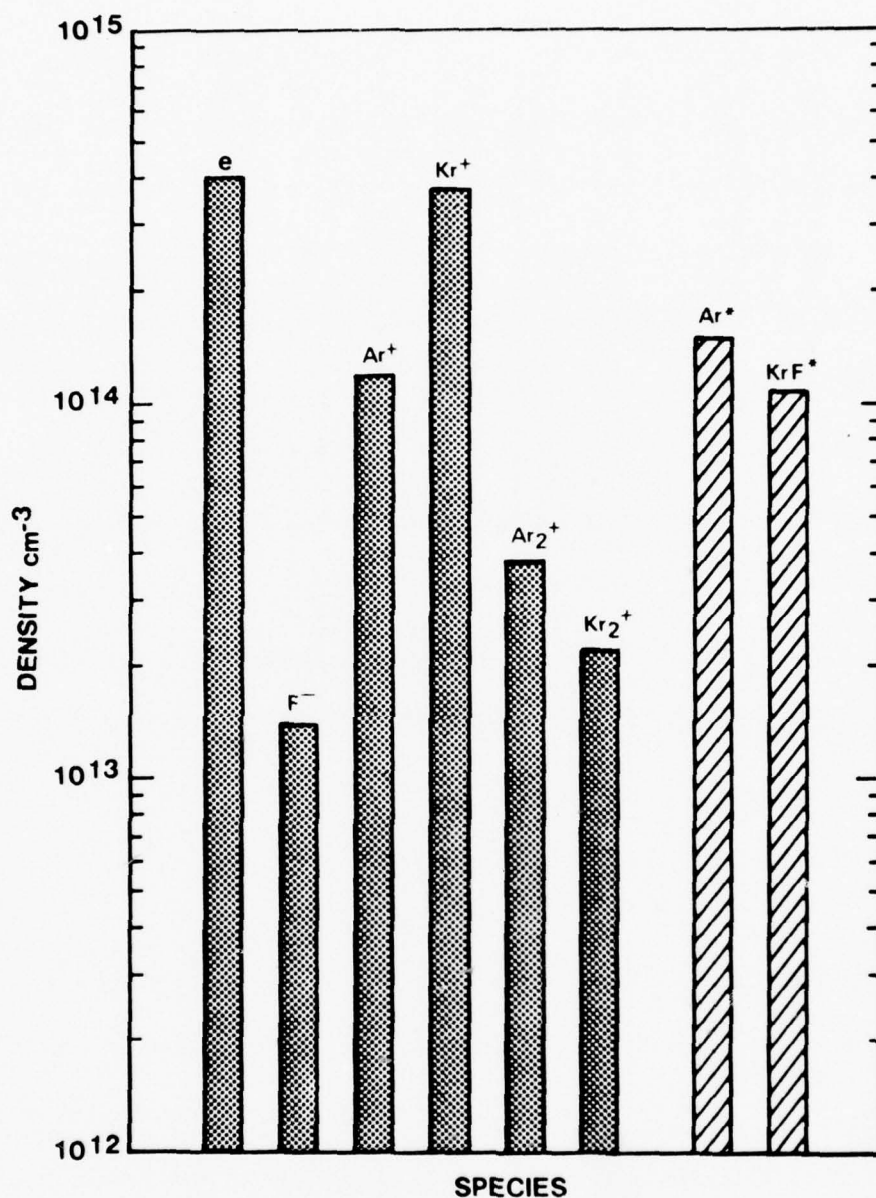
Figure 3. Computed quasi-steady charged particle densities in an electron beam pumped Ar-Kr-F$_2$ (0.95-0.05-0.002) mixture at atmospheric pressure.

at atmospheric pressure. The densities of Ar metastables and KrF* are also shown for purposes of comparison. These data show that for typical conditions the densities of excited states and charged particles are comparable in magnitude. Similar calculations for a range of circumstances indicate that the fractional ionization and fractional excitation densities are both typically in the range 10^{-6}-10^{-4}. These levels of fractional ionization and excitation are relatively high, with the result that collisions between charged particles and between charged particles and excited states are very important. Thus, these processes have been included throughout this analysis.

For the conditions of Fig. 3 the total e-beam power density deposited in gas was about 72 kWcm^{-3} and the small signal gain was found to be approximately 1% cm^{-1}. In addition, it is particularly useful to determine the fractional power which is $\underline{\text{potentially}}$ $\underline{\text{available}}$ for conversion to optical power. Herein, this measure of maximum attainable efficiency will be defined in the following manner:

$$\eta_p = \frac{(KrF^* \text{ pumping rate}) \, h\nu}{[Ar]S_E u_i + JE}, \qquad (1)$$

where all the processes contributing to the volumetric rate of KrF* formation are included in the numerator. Also, S_E is the rate of electron-ion pair production, u_i is the energy required to produce an electron-ion pair, JE is the discharge power density (zero for the conditions of Fig. 3), and $h\nu$ is the photon energy of the KrF* laser transition. Thus, on this basis the quantum efficiency is included in the definition of η_p, which in effect, represents the fraction of the total power potentially recoverable from the reaction $KrF^* + h\nu \rightarrow Kr + F + 2h\nu$. For the

12

conditions of Fig. 3, η_p was found to be 0.26, implying that the multiple energy transfer pathways in e-beam pumped systems as illustrated in Fig. 1 result in very efficient production of KrF[*]. This result is in good agreement with experimental observations.

The dimer ion concentrations Ar_2^+ and Kr_2^+ are likely to be of considerable importance because photodissociation of these species may be the dominant absorption of rare gas-halide laser radiation.[1] However, accurate computation of dimer ion density is very difficult at the present time. For the high pressure-low translational temperature conditions of interest, a fraction of the rare gas dimer ions are likely to be converted to trimers by way of three body reactions.[11,19] However, with the exception of the Xe_n^+ sequence[19] the relative equilibrium between dimers and trimers is unknown for the heavy rare gases. In the case of Xe_n^+, for example, the ratio Xe_3^+/Xe_2^+ is expected to be of order 10 at ambient temperature and pressure and is exceptionally sensitive to temperature.[19] Therefore, with the rare gas dimers as principal absorbers of laser radiation, the relative dimer-trimer fraction could be very important. Unfortunately, the equilibrium constant for this reaction is known reliably for Xe alone.[19] For this reason the influence of trimer ion formation has not yet been considered.

Excited State Concentrations

Shown in Fig. 4 are computed excited state densities in an externally sustained discharge for conditions otherwise similar to those of Fig. 1. For these conditions the total power density was also in the 70 to 75 kWcm^{-3} range, 2/3 of which was provided by the discharge field and 1/3 by the external source of ionization, i.e.,

DENSITY cm^{-3}

10^{14}

10^{13}

10^{12}

10^{11}

Ar*

Kr*

Ar$_2$*

Kr$_2$*

Ar F

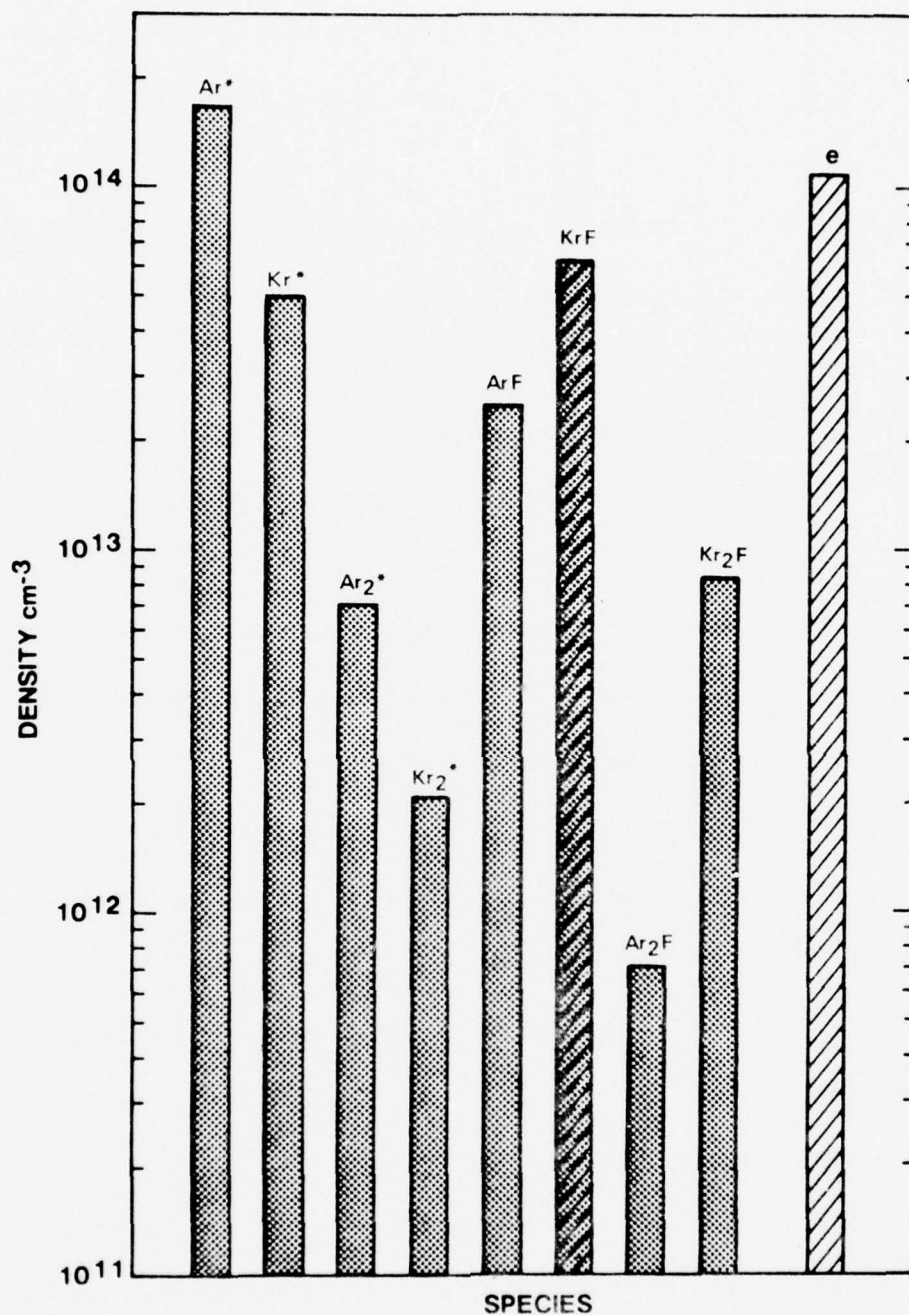Kr F

Ar$_2$F

Kr$_2$F

e

SPECIES

Figure 4. Computed quasi-steady excited state densities in an externally sustained, discharge pumped Ar-Kr-F$_2$ (0.95-0.05-0.005) mixture at atmospheric pressure. The value of E/n for these conditions was 1.0 x 10^{-16} Vcm^2 corresponding to an "electron temperature" of approximately 3.0 eV.

14

the discharge power enhancement factor[20], $JE([Ar]S_E u_i)^{-1}$, was 2. Under these circumstances the potential conversion efficiency as defined by Eq. (1) was found to be 0.18, while the small signal gain was approximately 0.65% cm^{-1}. It is interesting to note that although the total power density, efficiency and gain are nearly the same as in the case of pure e-beam pumping (Fig. 3), the total charged particle density (and presumably, therefore, the rare gas dimer ion density) is substantially lower with discharge pumping. This reflects a rather fundamental difference between e-beam pumping in which KrF* is produced by way of ion recombination channels (Fig. 1), and discharge pumping in which KrF* is produced by way of excited state reactions (Fig. 2). For this reason it appears that the density of dimer ion absorbers will be less in externally sustained discharges than in their electron-beam pumped counterparts under otherwise similar conditions.

D. KrF* Production Efficiency-Discharge Pumping

Examination of the tabular list of reactions discussed above suggests that there are numerous parasitic energy loss channels in rare gas-halide discharges. Yet calculations of discharge fractional power transfer show a surprising selectivity for the production of the KrF* excimer. In fact, the energy efficiency of KrF* production appears to be comparable to that of CO_2 and/or CO vibrational excitation in ir molecular laser discharges. Shown in Fig. 5 are the various fractional contributions to discharge fractional power transfer as a function of E/n in an externally sustained KrF laser discharge after quasi-steady conditions have been achieved. The energy transfer associated with all processes ultimately resulting in the formation of KrF* molecules has been included in the fraction
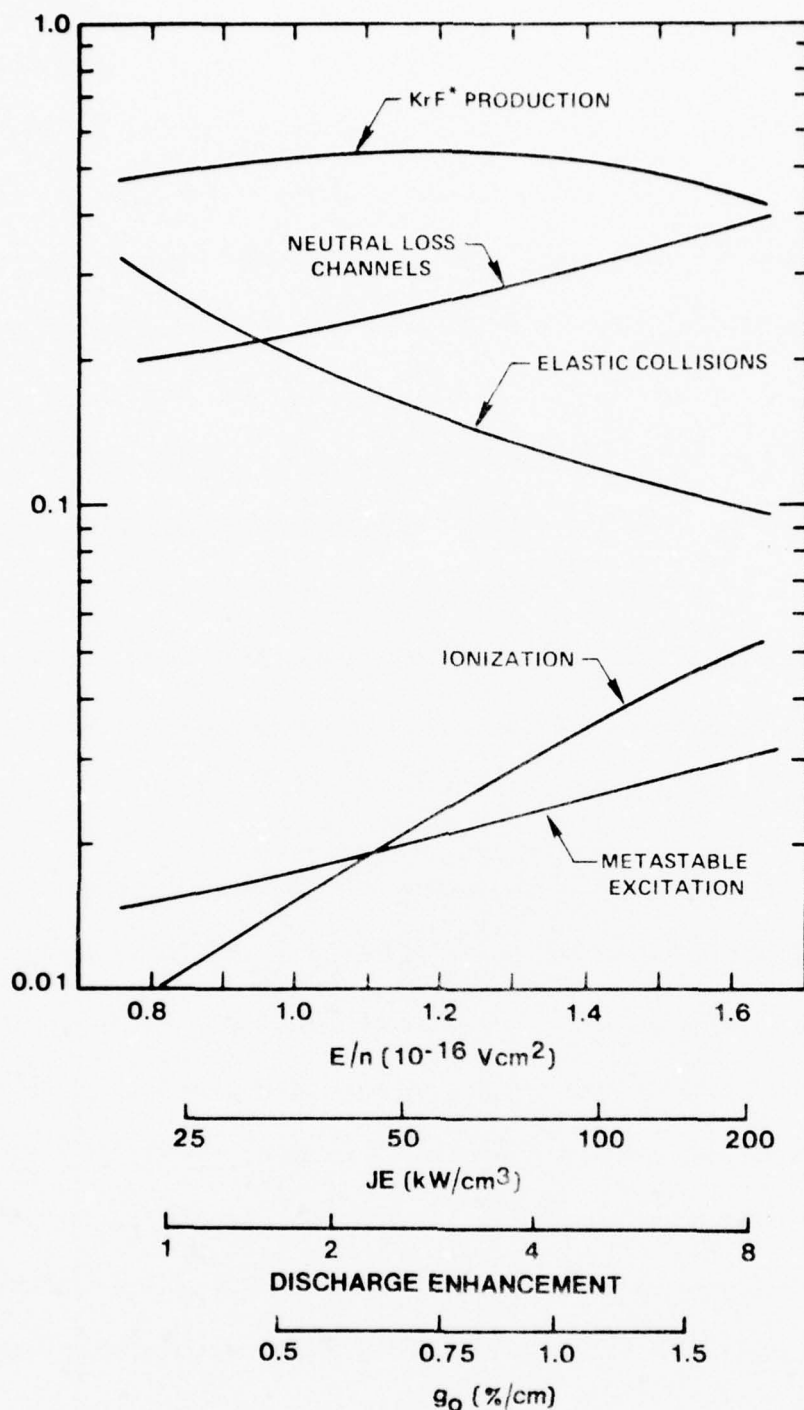
Figure 5. Fractional contributions to electron power transfer in an electron beam sustained Ar-Kr-F$_2$ (0.95-0.05-0.005) mixture at a pressure of one atmosphere presented as a function of E/n. Also shown for comparison are the discharge contribution to the total volumetric power density (JE), the discharge power enhancement, and the small signal gain. These data reflect quasi-steady conditions approximately 100 nsec after initiation of the discharge pulse.

16

attributed to KrF^* production, about half of which is potentially available for conversion to optical power. The following features of Fig. 5 are of particular importance: (1) the fractional power loss due to electron elastic collisions with ions and neutrals is always significant, i.e., $\gtrsim 10\%$; (2) the fractional power consumed by ionization of metastables and by direct ionization is also significant and increases with E/n, ultimately having a significant effect as plasma stability as will be discussed in subsequent sections; and (3) the overall efficiency with which discharge power is utilized in the production of KrF^* is very high and is relatively insensitive to E/n, a somewhat surprising result. It should be pointed out that the contribution of the discharge sustaining e-beam has not been included in the presentation of Fig. 5.

Gain and Potential Laser Efficiency-E/n Variation

Presented in Fig. 6 are the small signal gain and the overall potential electrical-optical conversion efficiency (Eq. 1) for the conditions of Fig. 5. The power density scale shown in this figure includes both the discharge power and the e-beam ionization power. Clearly, increases in E/n, and therefore, in discharge enhancement, result in increasing values of η_p and g_o, with the gain being a particularly sensitive function of E/n. This reflects the very strong dependence of Kr and Ar metastable production rate coefficients on E/n. It is important to note that the entire E/n range covered in Fig. 6 is not likely to be accessible due to the onset of plasma instability. For example, as E/n increases the contributions to electron production from direct ionization and ionization of metastables become increasingly important, circumstances which will be shown to contribute to instability
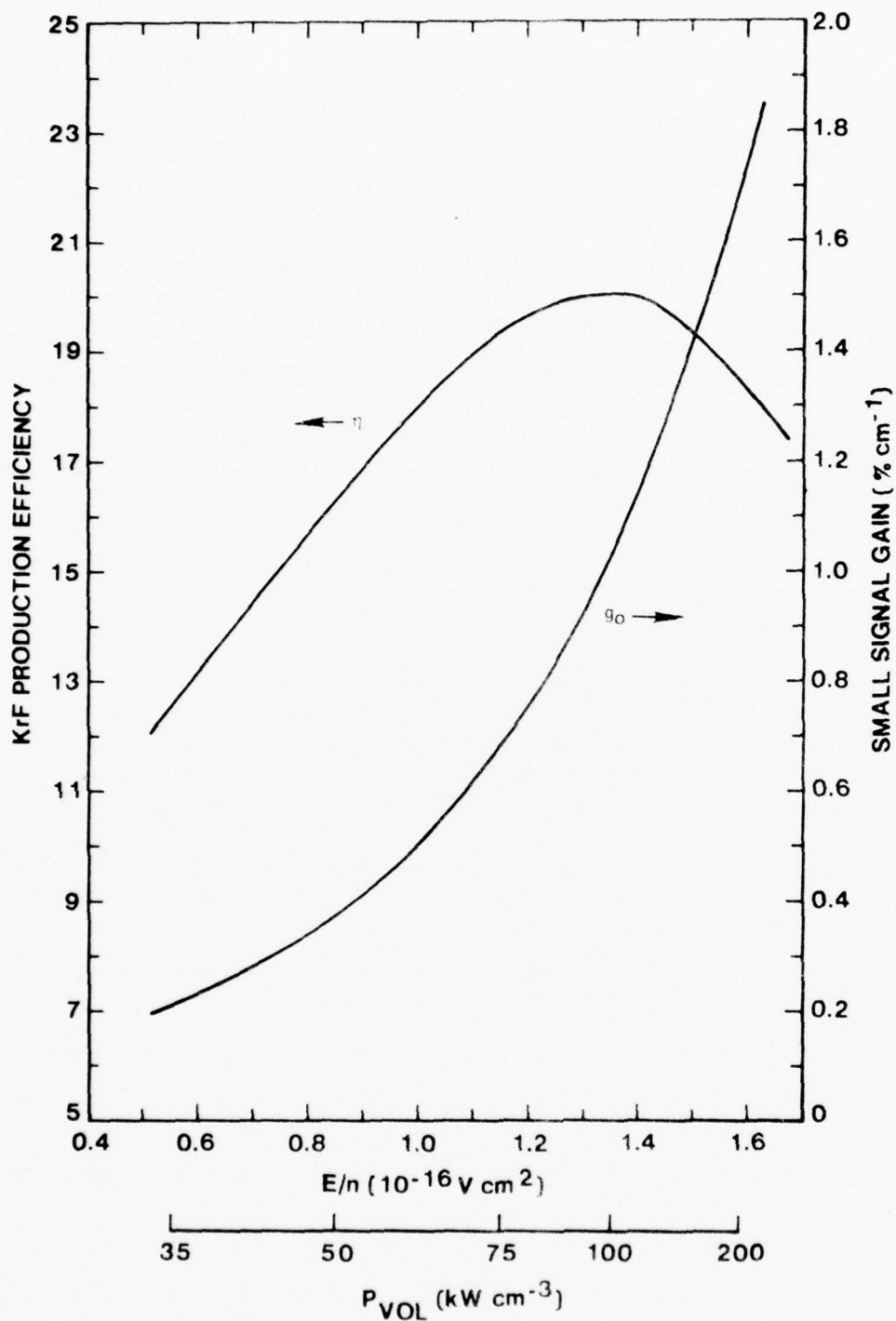
17

Figure 6. Small signal gain and potential electrical-optical conversion efficiency (Eq. 1) corresponding to the conditions of Fig. 5. The volumetric power density P_{vol} refers to the total power density, discharge plus electron-beam.

for E/n values in 1.4 to 1.6 x 10^{-16} Vcm^2 range for the conditions of the figure. For the lower values of E/n the potential efficiency remains relatively high but the gain falls rapidly due to the sharply reduced Ar and Kr excitation rates. Thus, there exists a rather narrow E/n window within which an efficient, stable discharge having adequate gain becomes possible.

Excited State Loss Processes

The production of excited states in rare gas-halide discharges is highly sensitive to E/n variations but is not particularly sensitive to variations in total pressure. However, excited state loss processes are highly pressure sensitive and are relatively unaffected by E/n changes. In fact, rare gas-halide lasers have been operated successfully only within the approximate range 0.3-3.0 atm. The reasons for this become apparent upon examination of the pressure dependence of the various contributions to excited state loss processes. Presented in Figs. 7 and 8 are the fractional contributions to the loss of Ar metastables and KrF*, respectively, for externally sustained discharge conditions. In these calculations the external ionization source was fixed with the result that the electron density is sensibly constant at a value of approximately 10^{14} cm^{-3} since both electron production and loss are proportional to pressure. However, this implies a fractional ionization change of over an order-of-magnitude over the pressure range shown in Figs. 7 and 8, electron collisions being relatively more important than neutral collisions at low pressures and the reverse at high pressures.

The data in Fig. 7 show that as the pressure is reduced below 1 atm the loss of Ar metastables (the primary precursor excited state) due to electron excitation
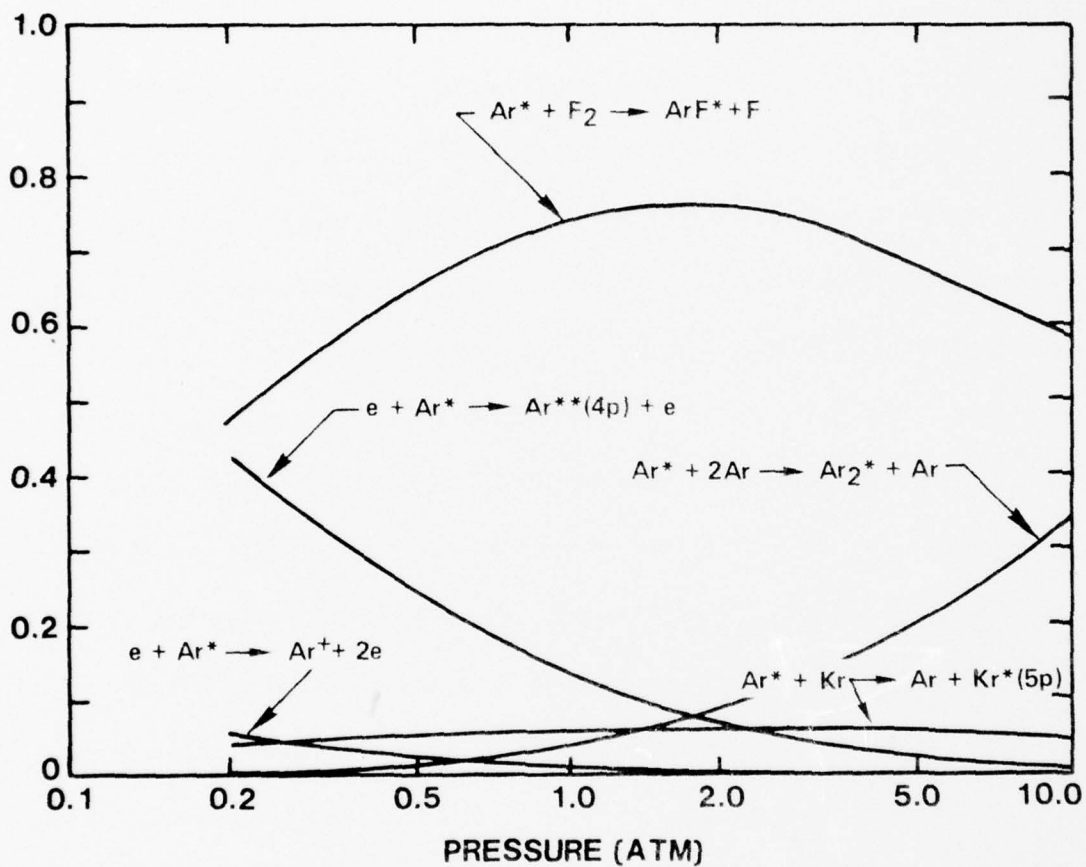
Figure 7. Fractional contributions to the loss of Ar metastables as a function of total pressure in an externally sustained, discharge pumped Ar-Kr-F$_2$ (0.95-0.05-0.005) mixture. These data are sensibly independent of E/n variations.

77-06-84-10

20

to the Ar p states becomes very important.[9] Although the Ar p states are optically connected to the s state metastable levels, at the pressures of interest here and with F_2 present in the mixture, the Ar p states are probably quenched by collisions. Such was assumed to be the case in the present analysis. On this basis it is found that although the power loss due to metastable excitation may be relatively small in some circumstances (e.g. Fig. 6), the loss of metastable atoms due to electron excitation to higher levels can be very important. In contrast, electron super-elastic collisions were found to be entirely insignificant compared to metastable excitation to higher levels and ionization of metastables. As the pressure is increased the loss of Ar^* by way of the ArF^* channel becomes dominant. Since ArF^* is also an important precursor of KrF^* (Fig. 2), a high conversion rate of Ar^* to ArF^* is desirable. If the proportion of F_2 in the mixture is reduced, the importance of Ar metastable loss due to electron collisions increases significantly relative to Ar conversion to ArF^*. For example, for F_2 fractions on the order of .001 or less, electron-Ar^* collisions dominate Ar^* loss for the conditions of Fig. 7. At pressures above about 2 atm the conversion of Ar to Ar_2^* becomes increasingly important. In addition, there are almost certainly other three-body quenching processes which come into play at the 10 atm level. In any case the computed maximum in the conversion of Ar^* to ArF^* at about 1 to 3 atm is in accord with experimental determination of optimum pressures and present understanding of KrF production mechanisms (Fig. 2).

The pressure dependence of KrF^* loss processes (Fig. 8) is even more striking, reflecting a transition from radiation domination at pressures of a few hundred
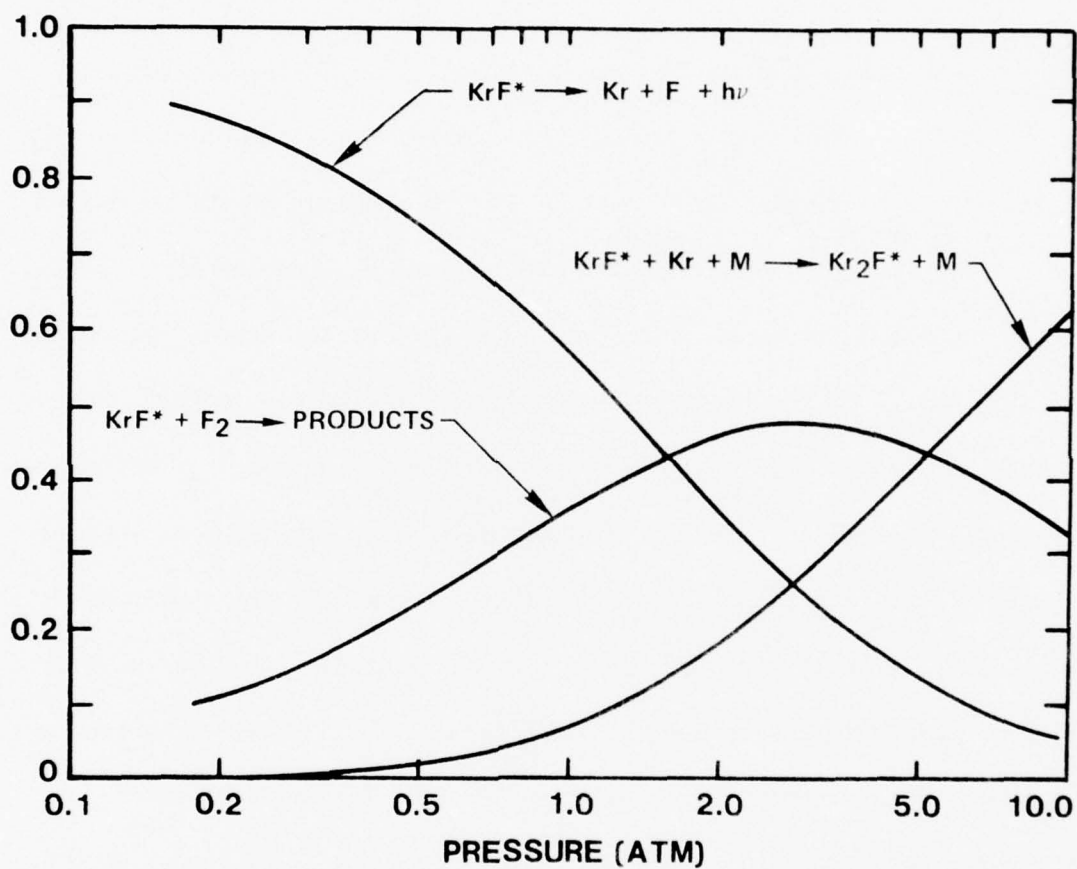
Figure 8. Fractional contributions to the loss of KrF* as a function of total pressure for the conditions of Fig. 7. These data are sensibly independent of E/n.

Torr to collision domination at a few atmospheres. At pressures of one atmosphere and below, loss of KrF^* is dominated by radiation, while three body conversion of KrF^* to Kr_2F^* dominates at pressures on the order of 10 atm, a result in good agreement with experimental observations.[1-5]

Gain and Potential Laser Efficiency-Pressure Variation

The trends exhibited by the data presented in Figs. 7 and 8 serve to explain the pressure dependence of the total potential efficiency and gain at constant E/n as shown in Fig. 9. While η_p is relatively high over the entire pressure range, gain is very sensitive to pressure variation. The variation in gain shown in this figure reflects the transition from a radiation dominated plasma in which KrF^* is quickly lost by way of spontaneous emission, to a plasma dominated by three-body collisions in which KrF^* is rapidly quenched.

E. Discharge Stability

To date most of the experimental results reported[1] have been obtained using electron-beam pumped rare gas-halide systems. However, there are numerous practical reasons why externally sustained discharge pumped systems having large energy enhancement[20] ratios ($\gtrsim 10$) would be desirable. Use of such a system should provide an element of control and substantially enhanced stability compared to a purely self-sustained discharge, while at the same time significantly reducing the considerable burdens associated with e-beam technology. For these reasons primary emphasis in the present study has been directed toward analysis of externally sustained rare gas-halide lasers. However, the experience obtained to date with such
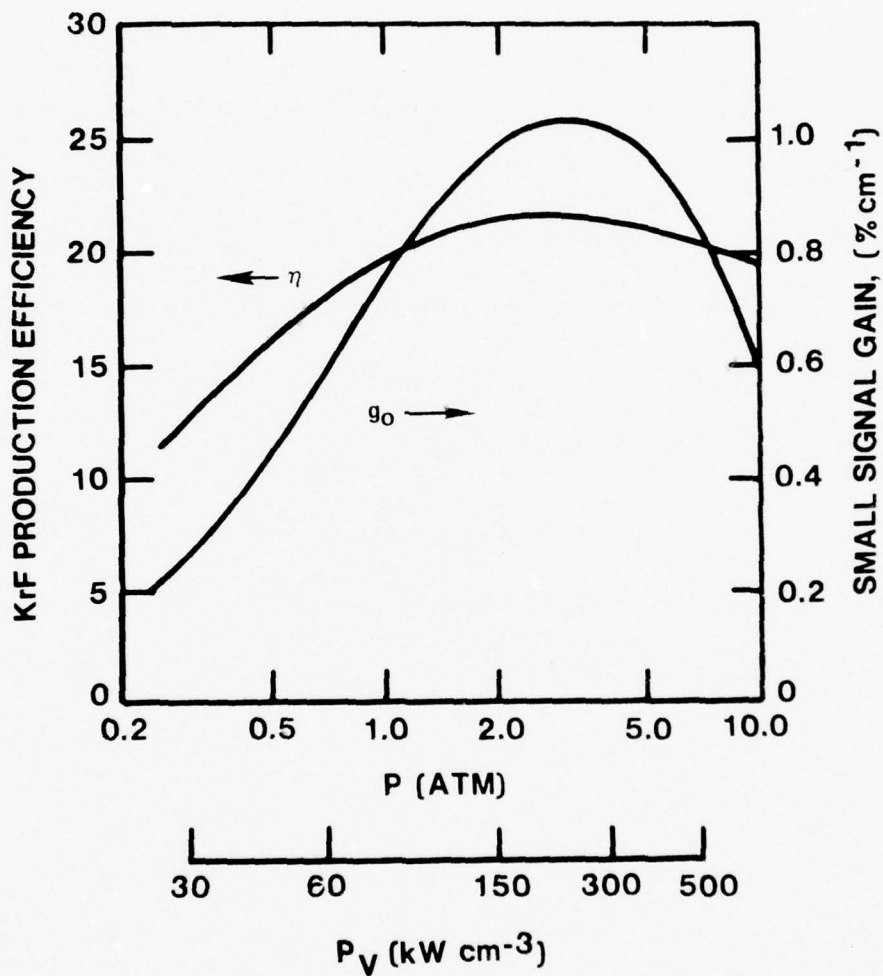
Figure 9. Small signal gain and potential electrical-optical conversion efficiency for the conditions of Figs. 7 and 8 and an E/n value of 1.2 x 10^{-16} Vcm^2.

systems[4] has been somewhat disappointing, the principal problem being the seemingly premature onset of instability which has limited stable discharge operation to times less than 100 nsec. This is in sharp contrast to the μsec duration electron-beam pumped rare-gas halide lasers reported recently.[21] Daugherty et al[20] have analyzed the stability of externally-sustained, attachment controlled discharges assuming that electrons are produced only by the external source and by ionization of metastable atoms. However, in the discussion to follow it will be shown that direct electron ionization of ground state atoms can also have a very important effect on stability by reducing the maximum E/n value at which stable discharges can be maintained.

Electron-Electron Collisions

The alkali-like electronic structure typical of rare gas metastable atoms and their low ionization energy combine to yield very large ionization rate coefficients ($\sim 10^{-8}$ sec^{-1}cm^3). These values are typically five orders of magnitude or more larger than those characteristic of direct ionization of ground state atoms in a weakly ionized discharge. Since the fractional concentration of metastable atoms is typically greater than 10^{-5}, it is usually concluded that direct ionization of atoms is entirely insignificant compared to metastable ionization. However, the plasma of a rare gas-halide laser discharge cannot be characterized as weakly ionized. Rather, for values of fractional ionization greater than about 10^{-6}, electron-electron collisions begin to exert a significant influence on ground state ionization rates (and metastable production rates as well) by way of their effect on the high energy portion of the electron energy distribution function. For this
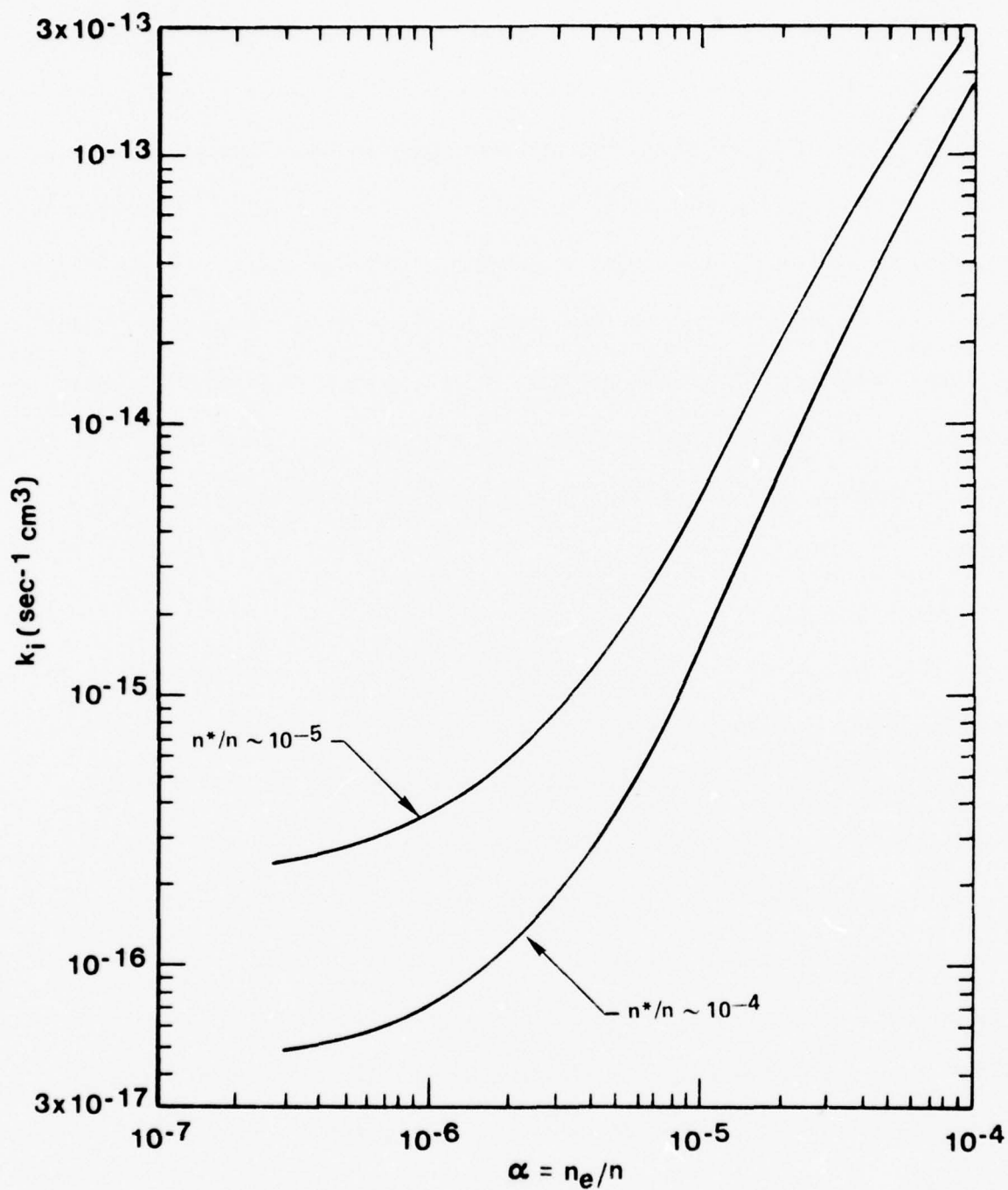
25

Figure 10. Computed ionization rate coefficient for ground state Ar atoms as a function of total excited state density and fractional ionization. These data are obtained for an E/n value of 1.0×10^{-16} Vcm^2 in an $Ar-Kr-F_2$ (0.95-0.05-0.005) mixture.

reason the dependence on fractional ionization of the electron distribution function and all relevant rate coefficients has been taken into account in the present analysis.

As an illustration of the effect of e-e collisions, Fig. 10 presents the computed ionization rate of Ar atoms in a KrF^* laser mixture as a function of fractional ionization for two values of fractional metastable concentration at a fixed value of E/n. These data show that as the fractional ionization increases from below 10^{-6} to above 10^{-5} there results about a two order of magnitude increase in the ionization rate. Since metastable concentration and electron density tend to increase together, the effect of rising fractional ionization tends to offset the tendency of the ionization (and excitation) rate to decrease as the metastable fraction increases. The primary point, however, is that direct ionization rates for ground state atoms can be orders of magnitude larger than is predicted if e-e collisions are neglected.

Charged Particle Production

Figure 11 shows the temporal evolution of the various fractional contributions to electron-ion pair production for a relatively high value of E/n (Figs. 5 and 6). As a consequence of the increased direct ionization rate caused by electron-electron collisions, the contribution of direct ionization is almost 25% initially. Thus, for these conditions the plasma is not sustained solely by the external source even when the metastable concentration is very low. As the metastable concentration grows, so does the fractional contribution of metastable ionization. However, for

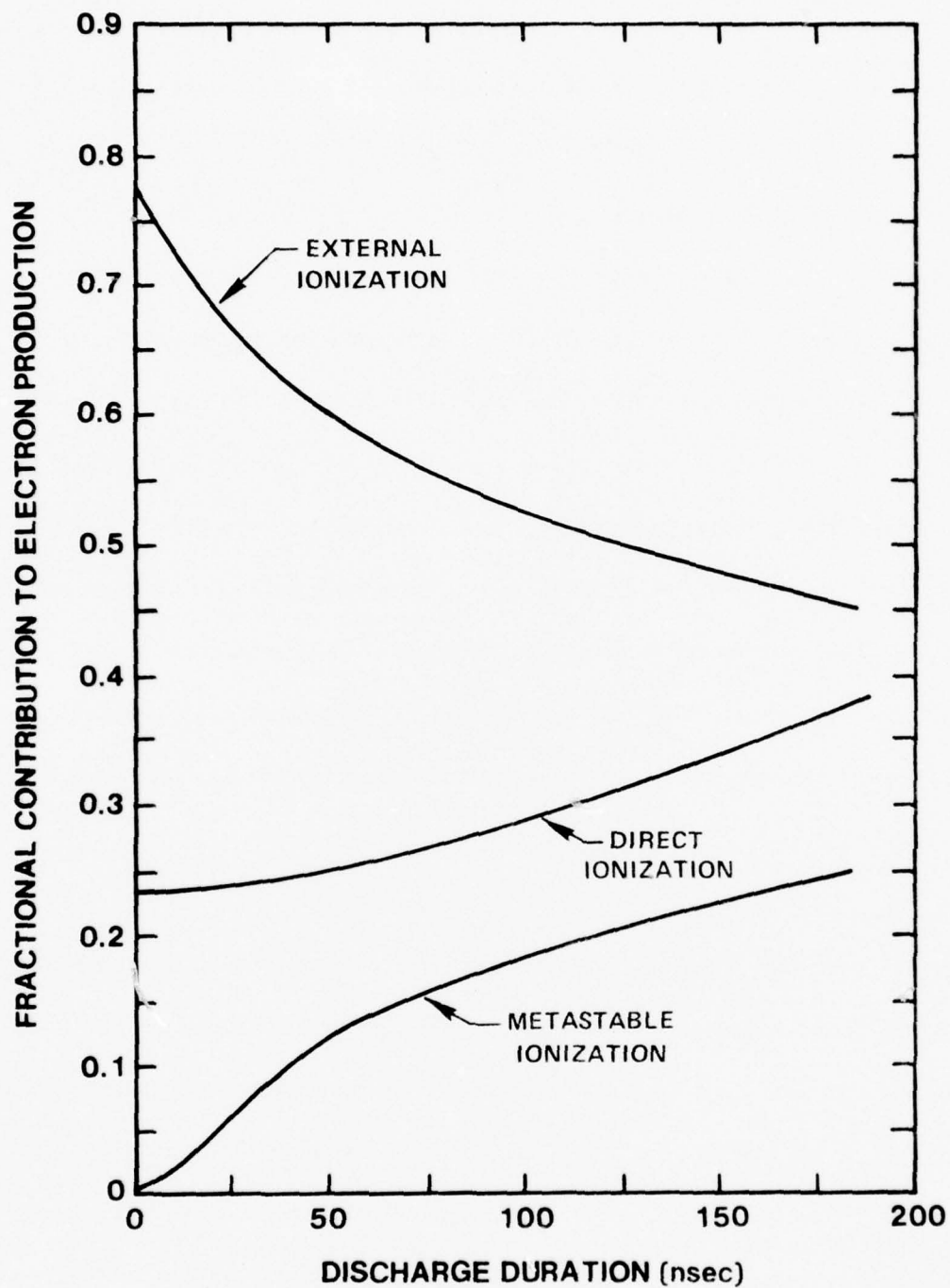27

Figure 11. Computed temporal change in the various fractional contributions to electron-ion pair production in an $Ar-Kr-F_2$ (0.95-0.05-0.005) mixture at atmospheric pressure and an E/n value of 1.6×10^{-16} Vcm^2.

77-06-84-2

28

the conditions of this example the direct and metastable contributions to the ionization process are always comparable.

Instability Growth Rate

Presented in Fig. 12 is the ionization instability growth (damping) rate computed for the conditions of Fig. 11 using procedures generally similar to those described elsewhere.[22] These results show that for this example the plasma becomes unstable (electron density disturbances are amplified) after a discharge duration of approximately 60 nsec, at which point the fractional contribution of metastable ionization (Fig. 11) is well below the 0.50 value originally suggested[20] as defining the stability boundary. Further, by the 100 nsec point the instability growth time (ν^{-1}) is only 10^{-7} sec and is decreasing rapidly. Thus, for these conditions a stable (i.e., diffuse) discharge could not be maintained for a time longer than about 100 nsec even in a perfectly uniform plasma. Although there remains much to be learned regarding the causes of instability in rare gas-halide discharges, these findings show that extraordinary care must be exercised in establishing operating parameters in order to achieve stable, externally sustained, rare gas-halide discharges.
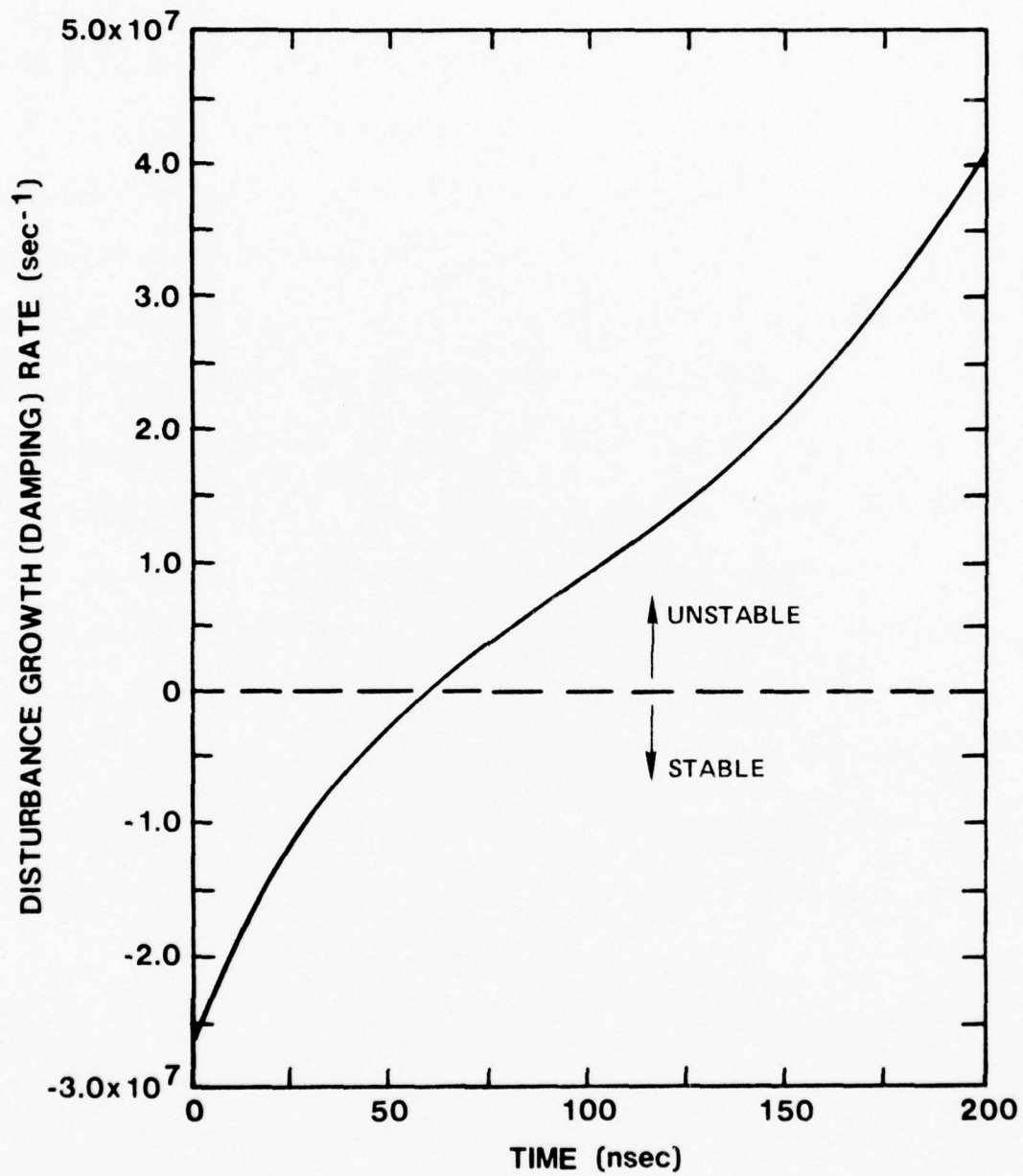
Figure 12. Approximate ionization instability growth (damping) rate computed for the conditions of Fig. 11.

III. ELECTRON-MOLECULE COLLISIONS

It is well known that as little as 1% of an atmospheric molecular species such as N_2 or CO_2 in a rare gas mixture can completely dominate electron energy transfer processes. Thus, although there exists almost no electron scattering data for halogen bearing molecules of the type used in rare gas-halide lasers, there is every reason to suppose that the presence of between 0.1 and 1% F_2 (or NF_3) will have some effect on electron kinetics other than by way of the well known disso-ciative attachment process.[6,10] In fact, variation of the F_2 fractional concen-tration in the calculations described in the previous section, in which electron energy loss due to collisions with F_2 was not included, has shown that both gain and KrF^* production efficiency should continue to increase with F_2 fraction in the 0.1 to 1.0% range, even though F_2 is assumed to quench all excited states with a rate coefficient of 10^{-9} sec^{-1}cm^3. However, this trend does not agree with experi-ments which show that for F_2 fractions above approximately 0.5%, laser performance is reduced. It is generally assumed that the reduction in laser output as the F_2 fraction approaches 1.0% is caused by F_2 excited state quenching processes. However, such behavior is also consistent with the onset of deleterious effects of e-F_2 collisions such as vibrational excitation, direct dissociation, and electronic excitation. Because of the potential importance of such processes to both the quasi-steady and stability characteristics of rare gas halide lasers, as part of this investigation considerable effort has been devoted to estimating the magnitude of e-F_2 cross-sections for vibrational and electronic excitation.

A. Vibrational Excitation-Dissociative Attachment

Theory

Electron-F_2 vibrational excitation cross-sections have been estimated by fitting resonance scattering theory[23,24] to known dissociative attachment rate data. If the potential energy curve for the $^2\Sigma_u^+ F_2^-$ state crosses the F_2 ground state near the equilibrium internuclear separation of the latter[25], there exists the possibility of a low energy shape resonance giving rise to dissociative attachment and vibrational excitation. In the resonance scattering model, the bombarding electron is temporarily trapped behind a potential barrier due mainly to the electron's orbital angular momentum, leading to a compound state or temporary negative ion. The electron can then tunnel out through the centrifugal barrier, leading to elastic or inelastic excitation of the target F_2, or it can be permanently trapped if the nuclei separate to the stabilization distance R_s (Fig. 13) where re-emission is energetically impossible. The latter situation corresponds to dissociative attachment. By using the compound state theory, the cross-sections for vibrational excitation and dissociative attachment can be calculated simultaneously. In F_2 the lowest unfilled orbital is $\sigma_u 2p$, which suggests a p-wave centrifugal barrier and a non-degenerate compound state in which the extra electron has zero component of angular momentum about the internuclear axis.

The details of the method applied in this analysis are presented elsewhere,[23,24] with emphasis directed toward N_2 and N_2O. Thus, only the highlights of the theory and those aspects relevant to F_2 are discussed here.
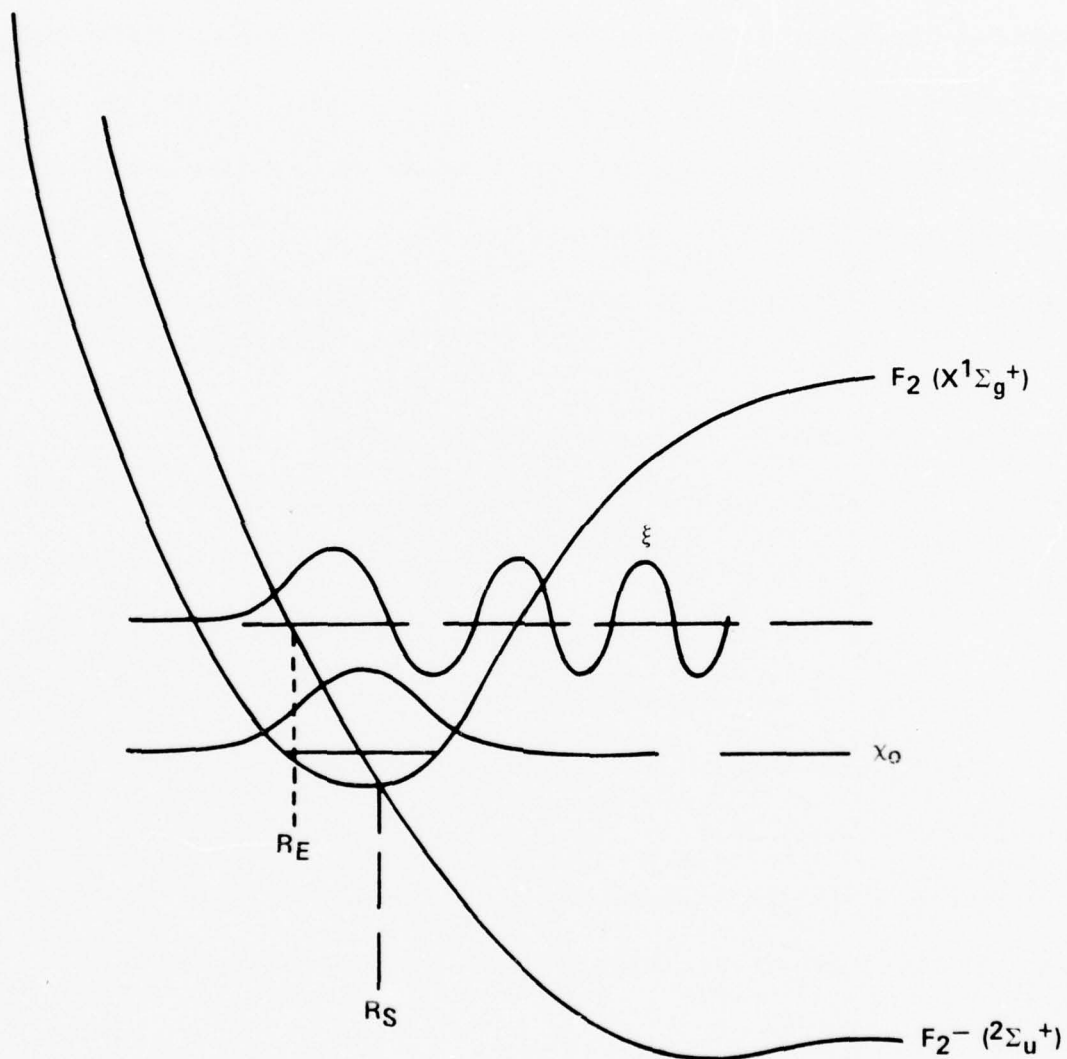
32

Figure 13. Schematic representation of dissociative attachment process. Wave function of negative ion, ξ, decays due to autoionization in region $R < R_s$. For $R \geq R_s$, negative ion is stabilized against electron emission, and ξ oscillates with constant amplitude.

33

Formally, a nuclear wave equation is solved in terms of a complex local potential for the compound state, F_2^- $(^2\Sigma_u^+)$. Because little is known about the real and imaginary parts of the compound state potential, these are treated as parameters. Adjustments are made to the potential parameters in a trial-and-error fashion until the predicted attachment cross-sections reproduce experimental rate constants for this process. Vibrational excitation cross-sections are then calculated from an overlap integral involving the compound state nuclear wave function and the target excited state vibrational wave function ($v \geq 1$). This process will give credible results only if the "best fit" potential parameters are physically realistic.

Calculations for F_2 differ from those reported[23] for N_2 in several relatively minor respects. Because the assumed F_2 resonance is $p\sigma$, the barrier penetration factor required for the calculation of the resonance width must be the expression appropriate to a p-wave, and the vibrational excitation cross-section is divided by a factor of two because the compound state is non-degenerate (see Eqs. 8 and 12 in Ref. 23). The boundary condition at infinite internuclear separation is changed from bound state to outgoing wave.

The nuclear wave equation is based upon the adiabatic and local potential approximations. Exchange and spin dependent forces are neglected, leading to:

$$\{- \frac{\hbar^2}{2M} \frac{\partial^2}{\partial R^2} + W(R) - E\} \xi = \zeta'(R) \chi_0(R) \tag{2}$$

where $- \frac{\hbar^2}{2M} \frac{\partial^2}{\partial R^2}$ is the kinetic energy operator for the nuclei; $W(R)$ is the electronic energy of the compound state, E is the total collision energy; ξ is the wave function

of the nuclei; $\zeta'(R)$ is an entry amplitude for the incident electron, and $\chi_o(R)$ is the vibrational wave function of the target. The compound state energy is represented by:

$$W(R) = E^-(R) - \frac{1}{2} i \; \Gamma(R)$$

where $\Gamma(R)$ is the autoionization rate multiplied by $\hbar$. The compound state electronic energy is complex for $R < R_s$ because the negative ion is unstable with respect to electron emission in this region. Γ is assumed to vary with R in accordance with the penetrability of a p-wave centrifugal barrier:

$$\Gamma(R) = \frac{2\gamma \; (k(R)\rho)^3}{1 + (k(R)\rho)^2}$$

where $k(R)$ is the wave number of the emitted electron, ρ is the "radius" of the F_2^- ion, and γ is a parameter. The expression for the entry amplitude ζ' is as given in Ref. 23 (Eq. 14).

The dissociative attachment cross-section is given by the expression,[26]

$$\sigma_{DA} = \frac{V_N}{V_o} \; \frac{(2S^- + 1)}{2(2S_o + 1)} \; \frac{1}{|I_o|^2} \; \lim_{R \to \infty} |\xi(R,E)|^2 \tag{3}$$

where V_N and V_o are the nuclear dissociation and incident electron velocities, respectively; $\frac{(2S^-+1)}{2(2S_o+1)}$ is a spin degeneracy factor (unity); and $|I_o|^2$ is the squared amplitude of the incident wave $(8\pi^3)^{-1}$. Cross-sections for the vibrational excitation processes,

$$e^- + F_2(v=0) \to e^- + F_2(v)$$

35
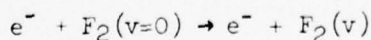
are calculated from the overlap integral,

$$\sigma_{ov} = \frac{V_v}{V_o} \frac{64\pi^5 \mu^2}{\hbar^4} \left| \int dR \; \chi_v^* \; \zeta\xi \right|^2 \tag{4}$$

where V_v is the velocity of the scattered electron, μ is the electron mass, χ_v is the excited vibrational state wave function, and ζ is an exit amplitude for the electron which is set equal to ζ'.

The boundary conditions applied to Eq. (2) are

$$\xi (0,E) = 0$$

$$\lim_{R \to \infty} \xi (R,E) = |\xi| \; e^{iKR}$$

$$\text{where } K^2 = \frac{2M}{\hbar^2} \lim_{R \to \infty} (E-E^-(R)) \tag{5}$$

Equation (2) with these boundary conditions is solved numerically by conventional finite different methods. Accuracy of the numerical solution is monitored by evaluating both sides of the equation

$$\frac{\hbar^2 K}{M} \lim_{R \to \infty} |\xi|^2 + \int \Gamma (R) \; |\xi|^2 \; dR$$

$$= - 2 \; \text{Im} \int \xi^* \; \zeta' \; \chi_o \; dR$$

which results from multiplying (2) by ξ^*, subtracting the complex conjugate, and integrating.

The most important approximation made in these calculations is that of a local potential. That is, the decay of the resonance is taken to be independent of final vibrational state. While this approximation will be valid for the relatively high electron energies of primary interest, it may be inaccurate at thermal energies[27]. Because the thermal electron attachment data influences the fitting procedure,

eventually it will be necessary to re-examine the low energy regime in terms of a non-local Γ. However, this approach results in an integro-differential nuclear wave equation which is more difficult to solve numerically.

The theory thus contains a number of adjustable parameters related to the complex electronic energy, $W(R)$. These parameters are varied to give a predicted dissociative attachment cross-section which, when integrated over an appropriate distribution of incident electron energies, has been found to compare favorably with the limited experimental dissociative attachment rate data which are available.

Calculated Results-Dissociative Attachment

The F_2 ground state potential energy curve was represented by a Morse potential with parameters taken from Ref. 28. Morse vibrational wave functions were also employed. The real part of the compound state energy was represented by a Taylor series for energies greater than the asymptotic value of -1.77 eV. This representation was chosen for convenience in making changes in slope and point of intersection (R_s) with the ground state. The only characteristic of the compound state curve that is of significance for $R > R_s$ is the asymptotic limit.

The heuristics of fitting the theory to the attachment rate data are of interest. A large number of calculations were performed for a range of compound state parameters that exhausted the physically realistic possibilities. For $R_s \geq R_o$ it was found that the predicted attachment rates were either too large or had peaks too far displaced from zero electron energy. It was possible to obtain an acceptable fit only for $R_s < R_o$. Good agreement was obtained for a particular set of parameters,

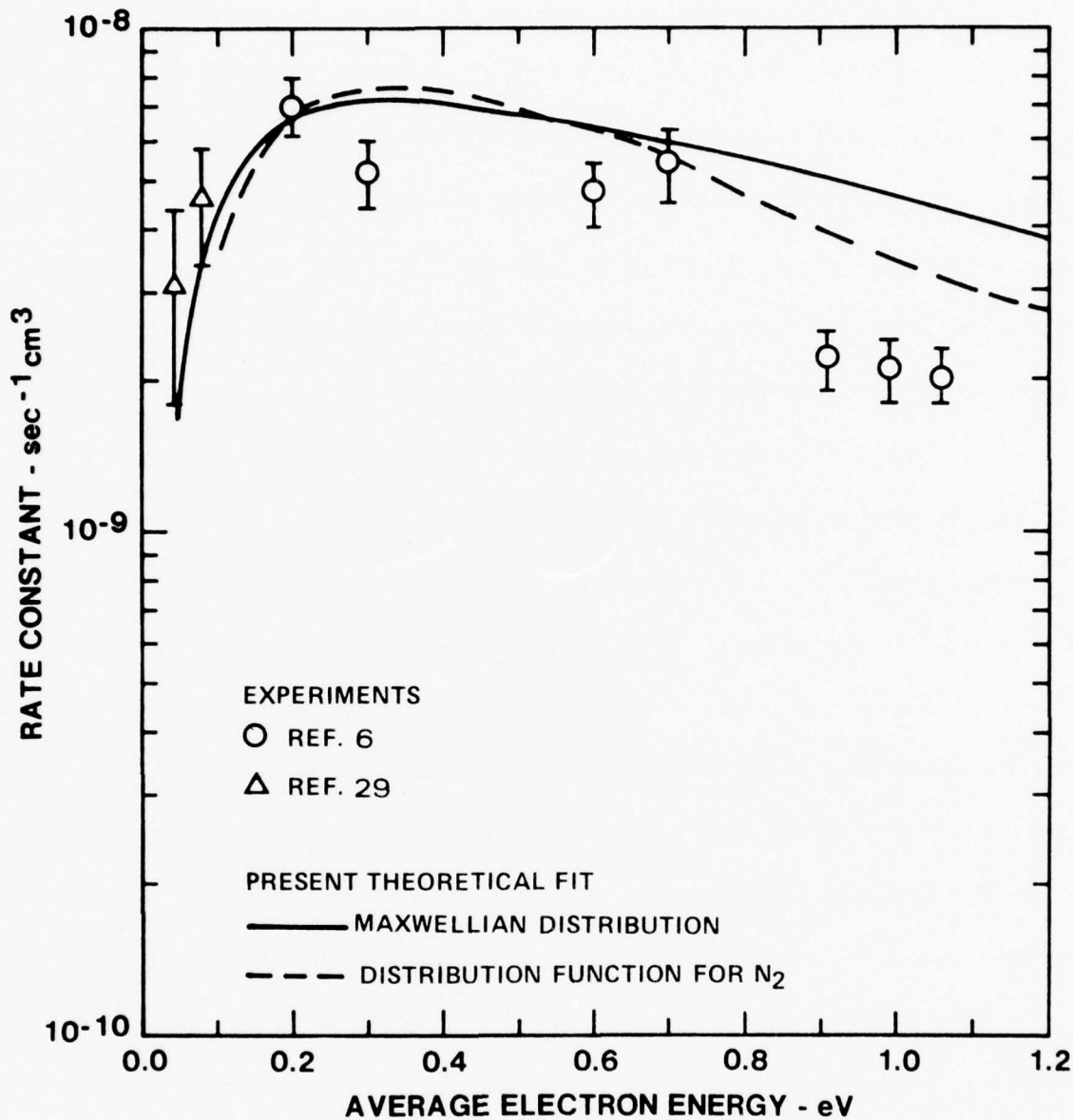Figure 14. Fit of resonance scattering theory to experimental attachment data. Solid curve represents rate constant calculated on basis of Maxwellian electron energy distribution. Dashed curve represents use of non-Maxwellian distribution function calculated for N_2-rich mixture. Theoretical attachment cross-section from which these rate constants are derived is given in Fig. 17.

77-06-84-23

38

as shown in Fig. 14. The real and imaginary parts of the negative ion potential which give this fit are shown in Figs. 15 and 16. As shown in Fig. 15, the curves cross about .1 a.u. from R_O. This result is consistent with ab initio potential calculations[25] in which a crossing at about 2.6 a.u. is predicted. The inferred $E^-(R)$ re-intersects the ground state at about 2.5 eV because best agreement with the attachment data was found to result from decreasing the slope of $E^-(R)$. The inferred $\Gamma(R)$ in Fig. 16 also is quite reasonable for a centrifugal barrier. Averaging Γ over the nuclear wave function yields values in the range .3-.4 eV.

The Maxwellian distribution used to calculate the attachment rates given by the solid line in Fig. 14 is an approximation. Better comparison with the experimental data is made by using an electron distribution function characteristic of the conditions in which the measurement was made. In particular, the data of Chen and co-workers[6,10] were obtained in N_2 buffer gas with F_2 mole fractions on the order of 10^{-3}. Accordingly, electron distribution functions for a representative N_2-F_2 mixture were calculated as a function of E/n. The result of using this non-Maxwellian distribution in the attachment rate calculation is shown as the dashed line in Fig. 14. It is apparent that better agreement with the experimental data is obtained using this more realistic distribution function. Departures from Maxwellian due to excitation of the N_2 vibrational mode become important at average electron energies around 1 eV, and cause the predicted attachment rate to decrease more rapidly with increasing energy. The fit exhibited in Fig. 14 is judged to be as good as is warranted by the scatter in the available experimental rate data.

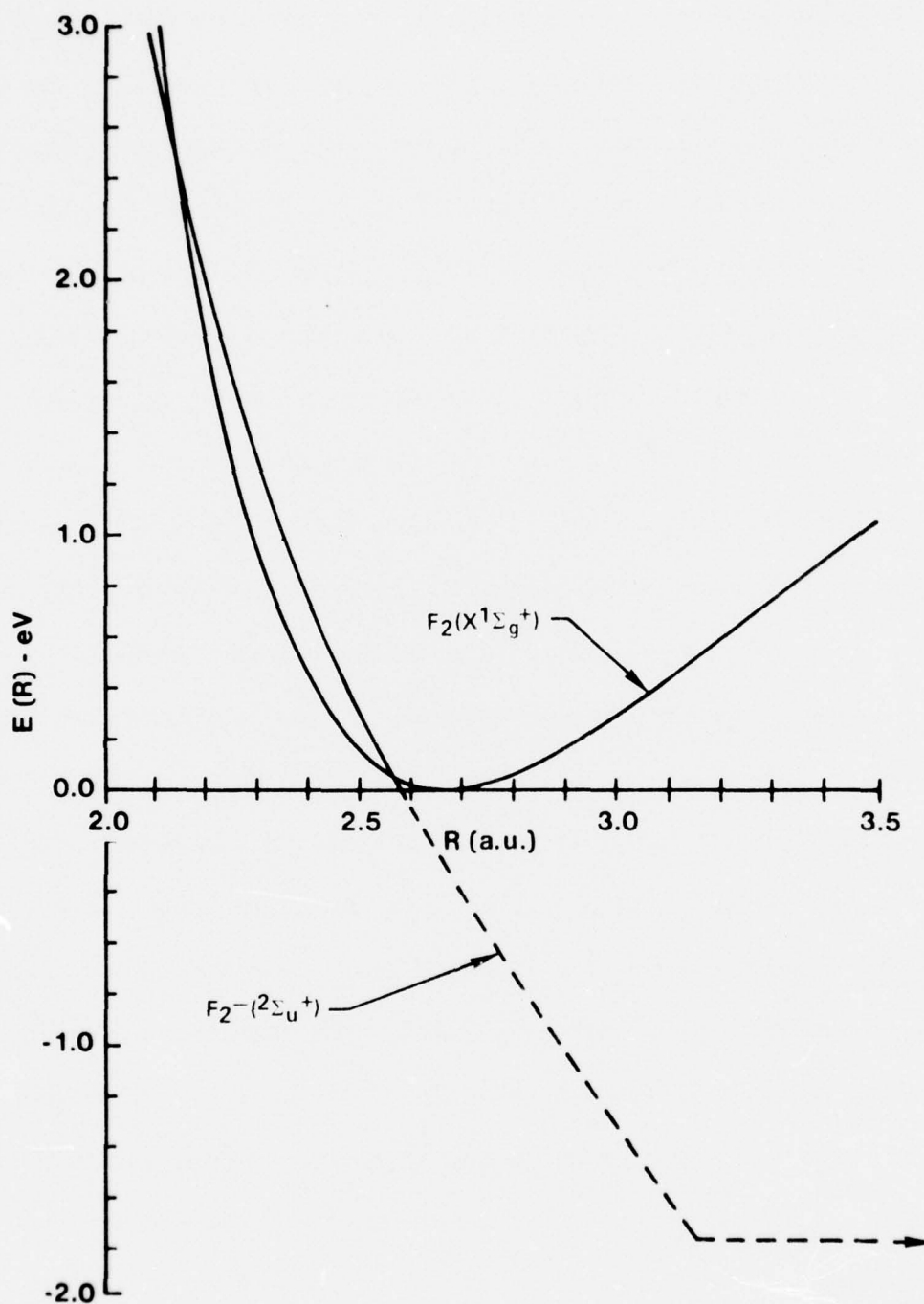Figure 15. Real part of best fit compound state potential; ground state represented by Morse potential. The compound state curve has the asymptotic value of -1.77 eV.

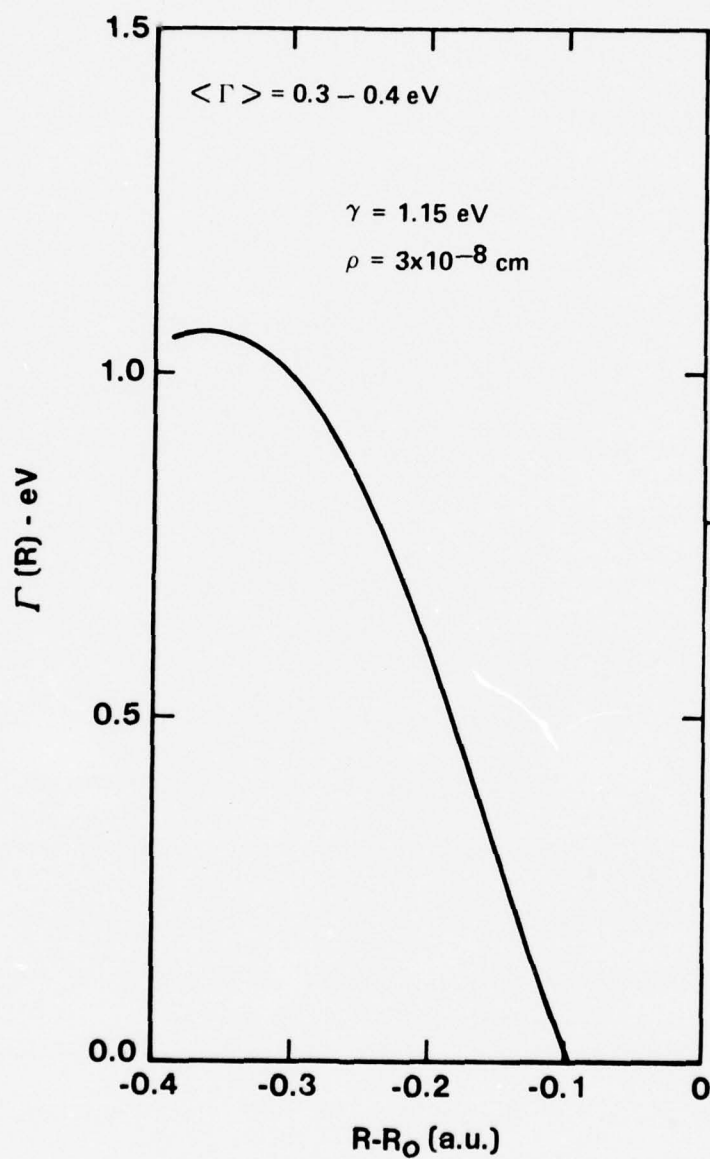Figure 16. Imaginary part of best fit compound state potential (the autoionization rate multiplied by $\hbar$). For small values of R, Γ varies as $(k(R)\rho)^3$. Averaging Γ over the resonance wave function yields values of 0.3-0.4 eV.

41

Attachment Cross-Section

The predicted attachment cross-section (Fig. 17) has a local maximum at about
.3 eV, and decreases by about an order of magnitude at 1 eV. It was found that as
Γ was reduced the local maximum and associated rate constant moved toward slightly
higher energy. This effect appears to be a consequence of the way in which the
entry amplitude, ζ', approaches zero as $R \rightarrow R_s$. At low Γ, increased capture at
slightly higher energies dominates a decreasing survival factor. As Γ is increased,
the peak does move toward zero energy, with diminishing survival factor at higher
energies becoming dominant. However, in this limit the width of the resonance
increases to the point where the predicted attachment rates at large energies are
too high. In the thermal energy limit the local Γ approximation becomes doubtful,
and a proper analysis of the very low energy attachment cross-section will have to
await a non-local Γ calculation.

If the compound state potential given in Figs. 15 and 16 is correct, the
dissociative attachment cross-section is likely to have a strong dependence on the
vibrational quantum state of the target F_2 molecule. Replacing the $v = 0$ wave
function on the right hand side of Eq. 2 with an excited state target wave function
and modifying the collision energy make it possible to calculate the v-dependence
of the attachment rate. The results of such calculations are presented in Fig. 18,
which shows the rates for $v = 0$, 1, and 2. The predicted v dependence is very
strong, with the peak attachment rate increasing by about a factor of five from
$v = 0$ to $v = 2$. It is not known to what extent this result is a function of the
particular compound state parameters employed, but the prediction seems reasonable

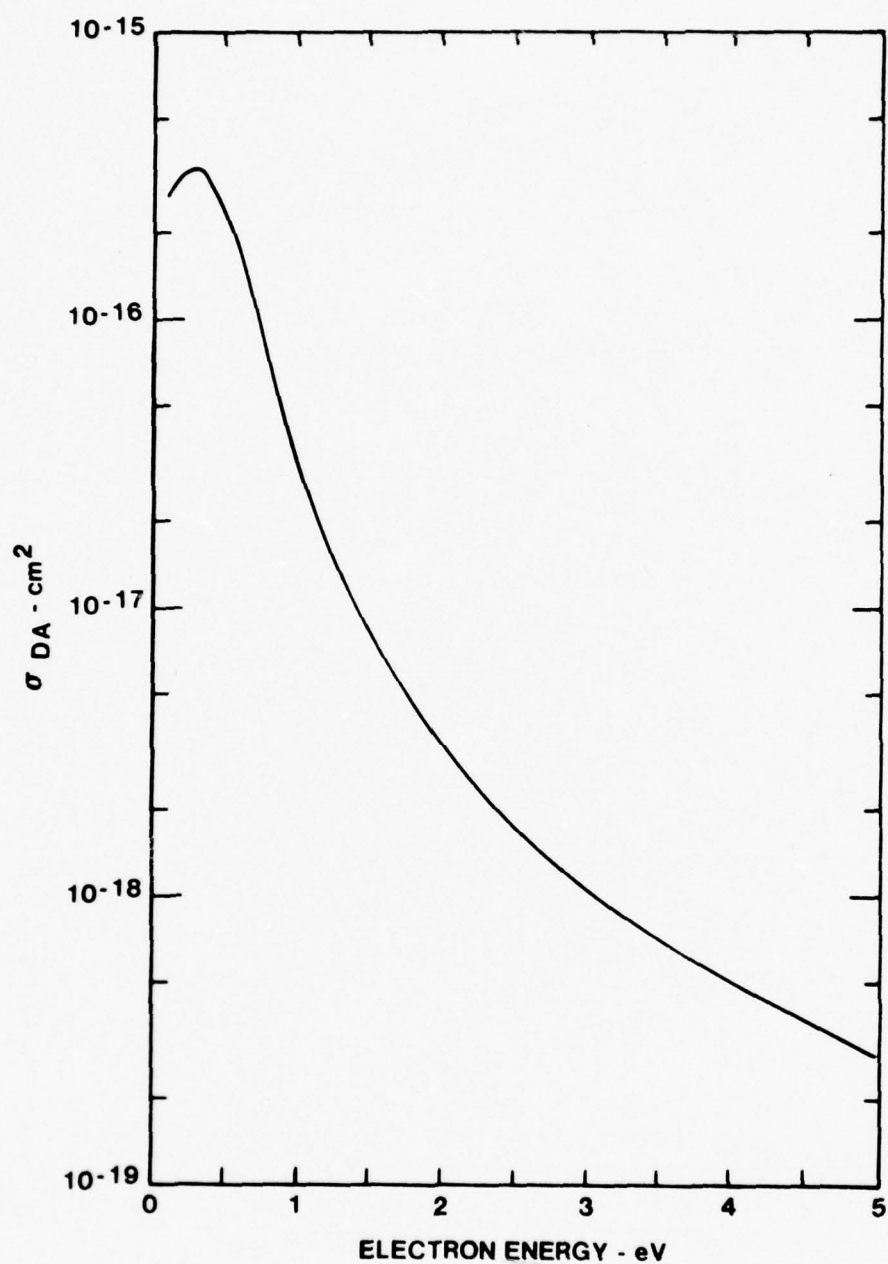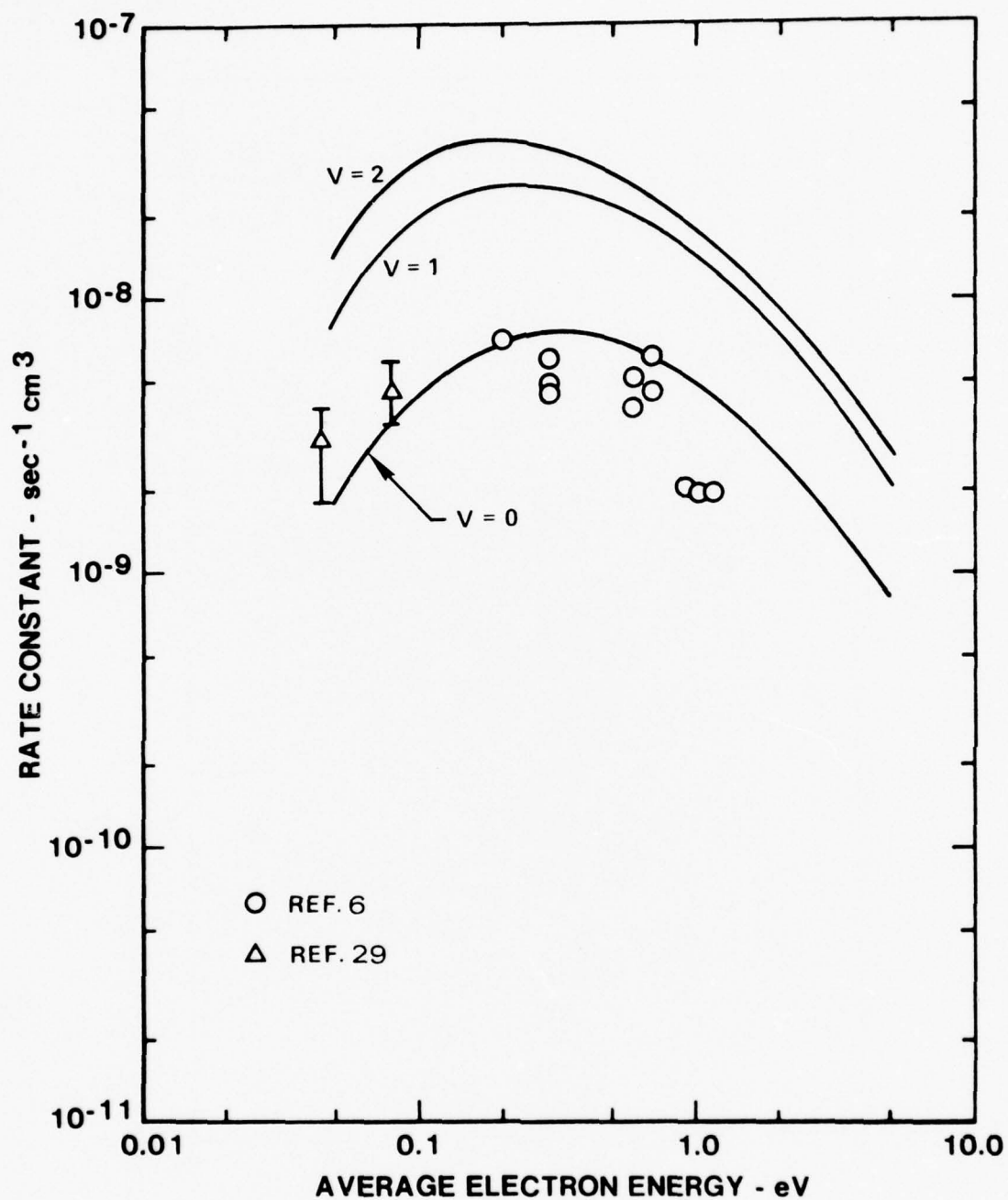Figure 17. Best fit attachment cross-section as a function of incident electron energy.

43

Figure 18. Predicted dependence of attachment rate on vibrational quantum number of target F_2. Rate constant calculated for Maxwellian energy distribution.

in view of a similar strong dependence in O_2.[30] The effect seems to be due less to survival factor arguments than to increased capture for the less compact excited state vibrational wave functions. An attachment rate with a significant dependence on vibrational quantum number could play an important role in long pulse rare gas-halide lasers, where the F_2 vibrational mode could be appreciably excited. Further, if this predicted dependence of attachment rate on quantum state is correct, the flowing afterglow measurements of Ref. 29 could contain excited state contributions.

Cross-Sections for Vibrational Excitation

Vibrational excitation cross-sections have been evaluated for the best fit attachment case. Figure 19 shows the calculated cross-sections for $v = 1, 4, 8$, and 12, and the sum of the cross-sections for excitation up to $v = 15$. The first vibrational state has a peak cross-section value of about 10^{-16} cm^2; at $v = 15$ the maximum has fallen to about .001 that of $v = 1$. Significant excitation of high-lying levels is predicted because this is a "strong coupling" case; the ratio of momentum imparted to the nuclei to the initial r.m.s. momentum

$$\frac{2a\ dE^-/dR}{\langle \Gamma \rangle}$$

is approximately unity. Here a is the vibrational amplitude of the ground state. Vibrational excitation cross-sections for F_2 show no structure (peaks and valleys) as a function of incident electron energy, in contrast to the situation in CO, N_2, O_2 and NO. In F_2, the compound state wave packet slides from the formation point (R_E) down the potential well and out to infinite internuclear separation. There is no turning point to the right to give a reflected wave as in the boomerang model[23], so that no interference between outgoing and reflected waves can occur.
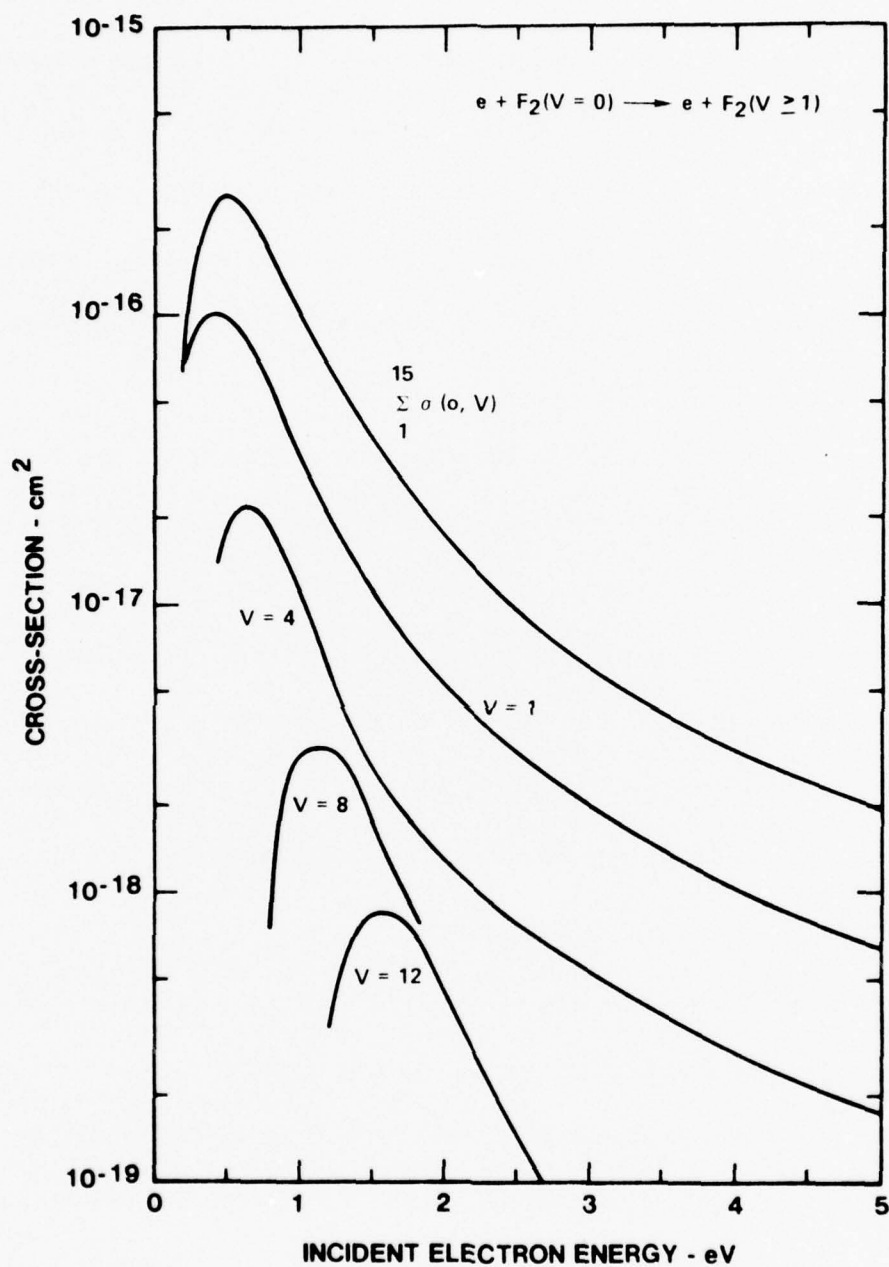
Figure 19.   Predicted vibrational excitation cross-sections.   Shown
are the individual cross-sections for excitation of v = 1, 4, 8 and 12,
and the total vibrational cross-section.

The resonant cross-sections shown in Fig. 19 are much larger than those calculated on the basis of direct scattering. Depending on the value assumed for the unknown quadrupole moment derivative, the Born approximation/quadrupole calculation gives a peak cross-section of 10^{-20}-10^{-19} cm^2 for the O-1 transition. Raman scattering data[31] yields a value of .21 a.u. for the matrix element of the derived polarizability tensor. Using this value in a polarization potential calculation[32] gives a peak cross-section of 10^{-18}-10^{-17}, depending on the value assumed for the cutoff parameter.

Because appreciable scatter exists in the attachment data, "fast" and "slow" fits have been carried out; results are presented in Fig. 20. These fits are derived from compound state potential parameters slightly different than in the best fit case. The associated total vibrational cross-sections are shown in Fig. 21. It is apparent that the uncertainty in the attachment data leads to a greater degree of uncertainty in the predicted vibrational cross-sections. The band of uncertainty is about an order of magnitude at higher electron energies. Thus, there is a clear need for more information on F_2 attachment to resolve uncertainties concerning both the magnitude and energy dependence (width) of the rate constant for this process.

The theory would be improved at thermal energies by employing a non-local Γ formulation. In reality, the term $\Gamma(R)\xi(R)$ in Eq. 2 should be a sum of terms representing negative ion decay to different vibrational states. The ionization rate to a particular vibrational state should reflect the fact that the energy of
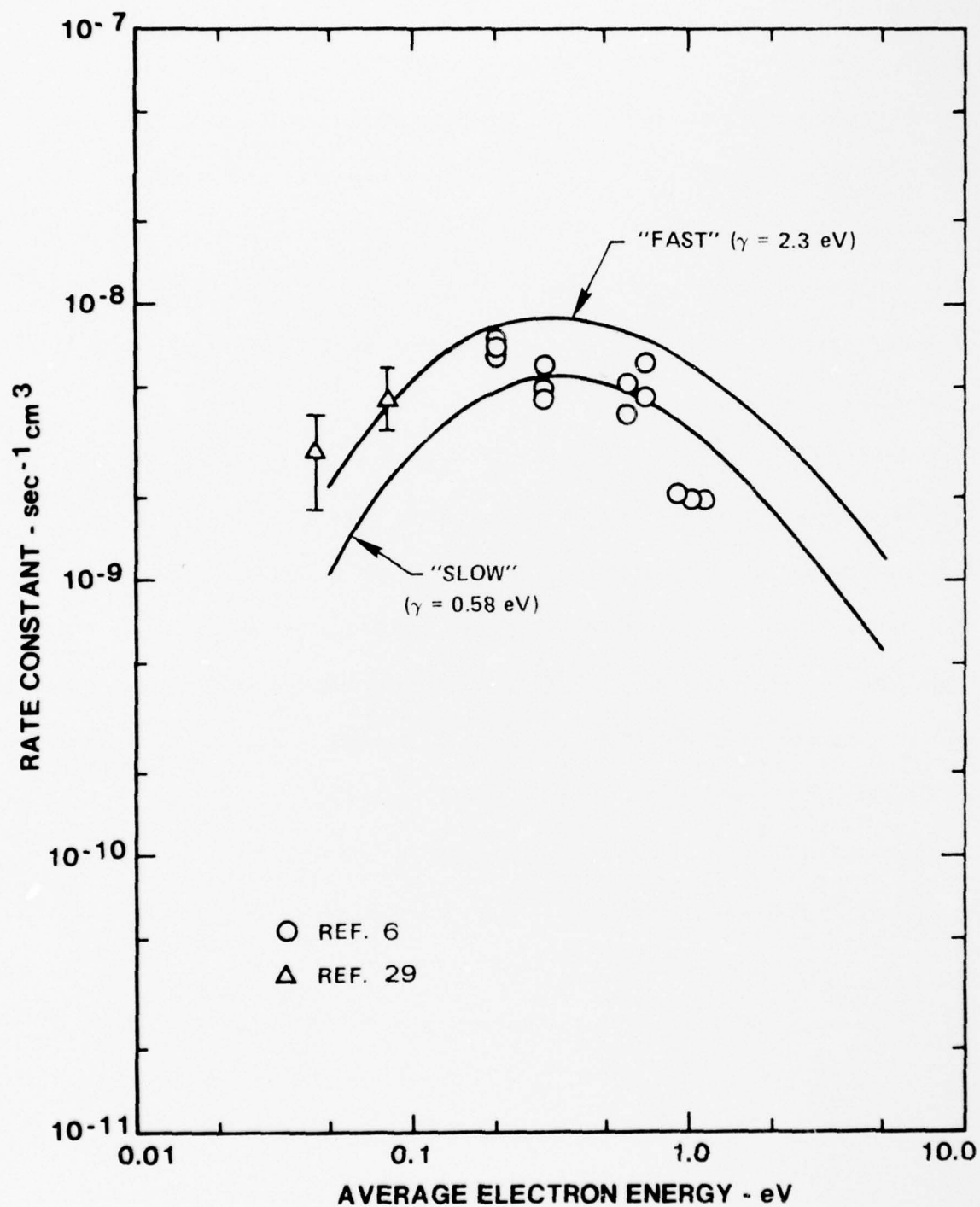
47

Figure 20. Alternative fits of resonance theory to attachment data. "Fast" and "slow" fits are calculated by multiplying and dividing the best fit Γ by a factor of two.

77-06-84-14

48
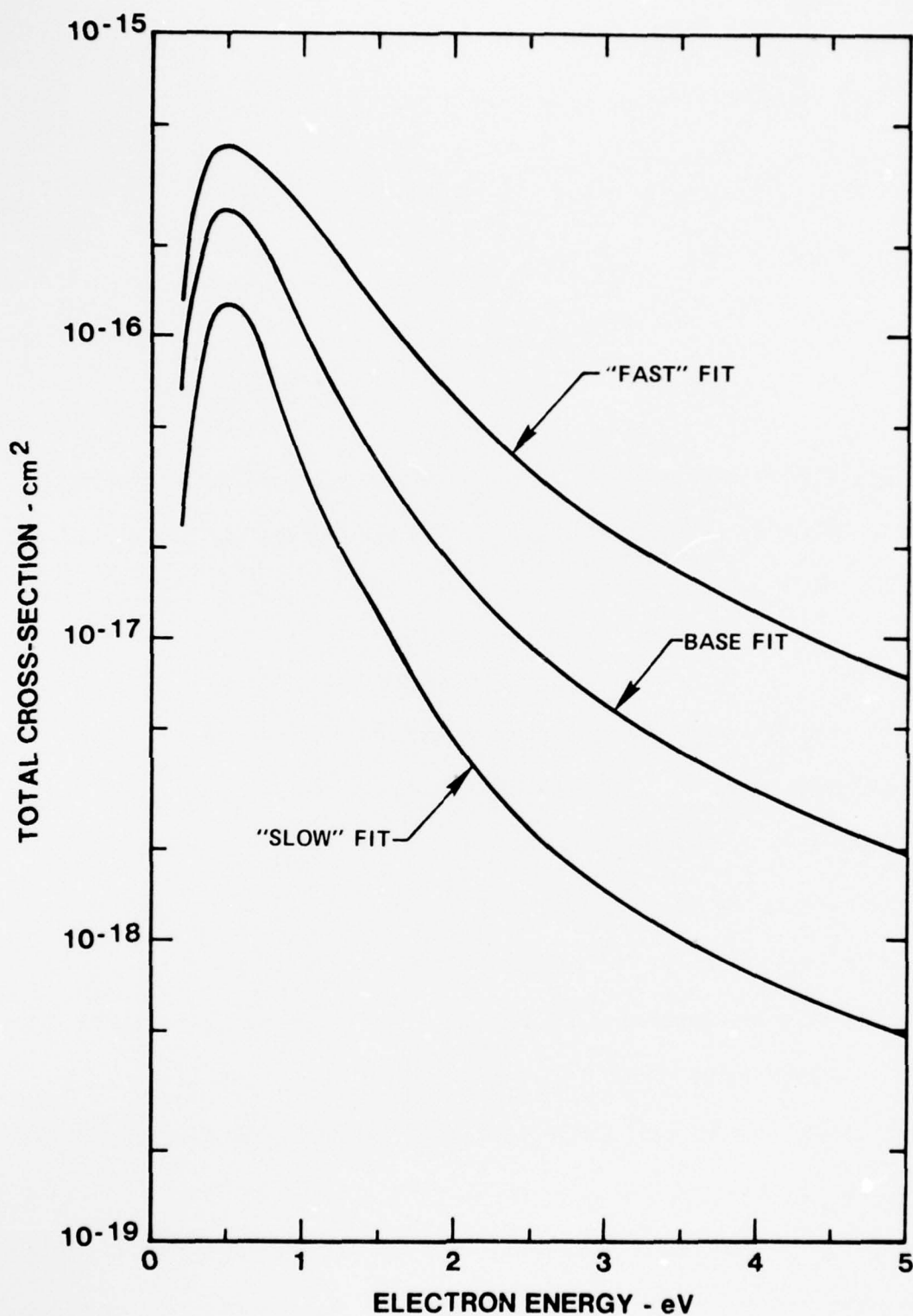
Figure 21. Sensitivity of total vibrational cross-section to variation in attachment rate fit.

49

the escaping electron is reduced by the vibrational excitation. Herzenberg[33] has shown that these effects can be accounted for by replacing the term $\Gamma(R)\xi(R)$ by:

$$\Sigma \; \chi_v(R) \; f(E-E_v) \int \; dR' \; \chi_v(R') \; \xi \; (R',E)$$

where the v summation extends over open channels and

$$f(E-E_v) = 2\gamma \; k_v\rho \; v_1 \; (k_v\rho)$$

$$k_v^2 = \frac{2\mu}{\hbar^2} \; (E-E_v)$$

The governing nuclear wave equation (2) thus becomes an integro-differential equation. Solution of this equation has not yet been attempted, although it could be solved by iteration, starting with the ξ-wave from the local Γ calculation.

B. Electronic Excitation-Dissociation

The vertical excitation energy[34] for the lowest F_2 electronic state ($^1\Pi_u$) is only 3.35 eV, well below the energy required for excitation of rare gas atoms. Also, although the cross-sections for excitation and ionization of the alkali-like rare-gas metastables are expected to be very large ($\sim 10^{-15}$ cm^2) for electron energy between 3.35 eV and threshold for atomic excitation (~ 10 eV), the density of metastable states will always be much less than that of the halogen-bearing molecule. Further, it has been shown herein that a resonance mechanism can give rise to vibrational cross-sections much larger than those expected from direct potential processes. In the same way, the cross-section for electron excitation of the repulsive F_2 ($^3\Pi_u$) state could be enhanced by a resonance process. Indeed there are several negative ion states F_2^- ($^2\Pi_g$), ($^2\Pi_u$) and ($^2\Sigma_g^+$) which may lie above

50

the dissociating F_2 $(^1\Pi_u)$ state in the vicinity of R_o. For these reasons it is likely that loss of electron energy due to dissociative excitation of F_2 is an important process for electrons in the 3 to 10 eV range.

Estimated e-F_2 Dissociation Cross-Section

Unfortunately, all prior experiments[35] directed toward investigation of F_2 dissociation have been sensitive only to the charged particles produced, e.g., F^+ and F^-. Thus, only the dissociative processes $e + F_2 \rightarrow F + F^-$ and $e + F_2 \rightarrow F^+ + F + 2e$ have been examined in any detail. Recently, data have been reported[10] relevant to F atom production in an externally sustained discharge-type experiment, which show evidence of enhanced F_2 dissociation in an E/n range high enough so that dissociative attachment should be decreasing (Fig. 14) and low enough so that dissociative ionization cannot occur. It was concluded,[10] however, that direct electron impact dissociation (or any of several other processes examined) could not be responsible for the observations. In view of the findings of the present study the F atom production data of Ref. 10 have been re-evaluated.

In order to assess the likelihood of electron dissociation contributing to the observations of Ref. 10, approximate electron energy distributions were computed for F_2 over the E/n range of the experiments[10] using the energy weighted vibrational cross-sections discussed in preceding paragraphs along with a constant momentum transfer cross-section of 10^{-15} cm^2. The e-F_2 dissociation cross-section was assumed to have an apparent threshold of 3.35 eV and its magnitude and shape above threshold were varied.
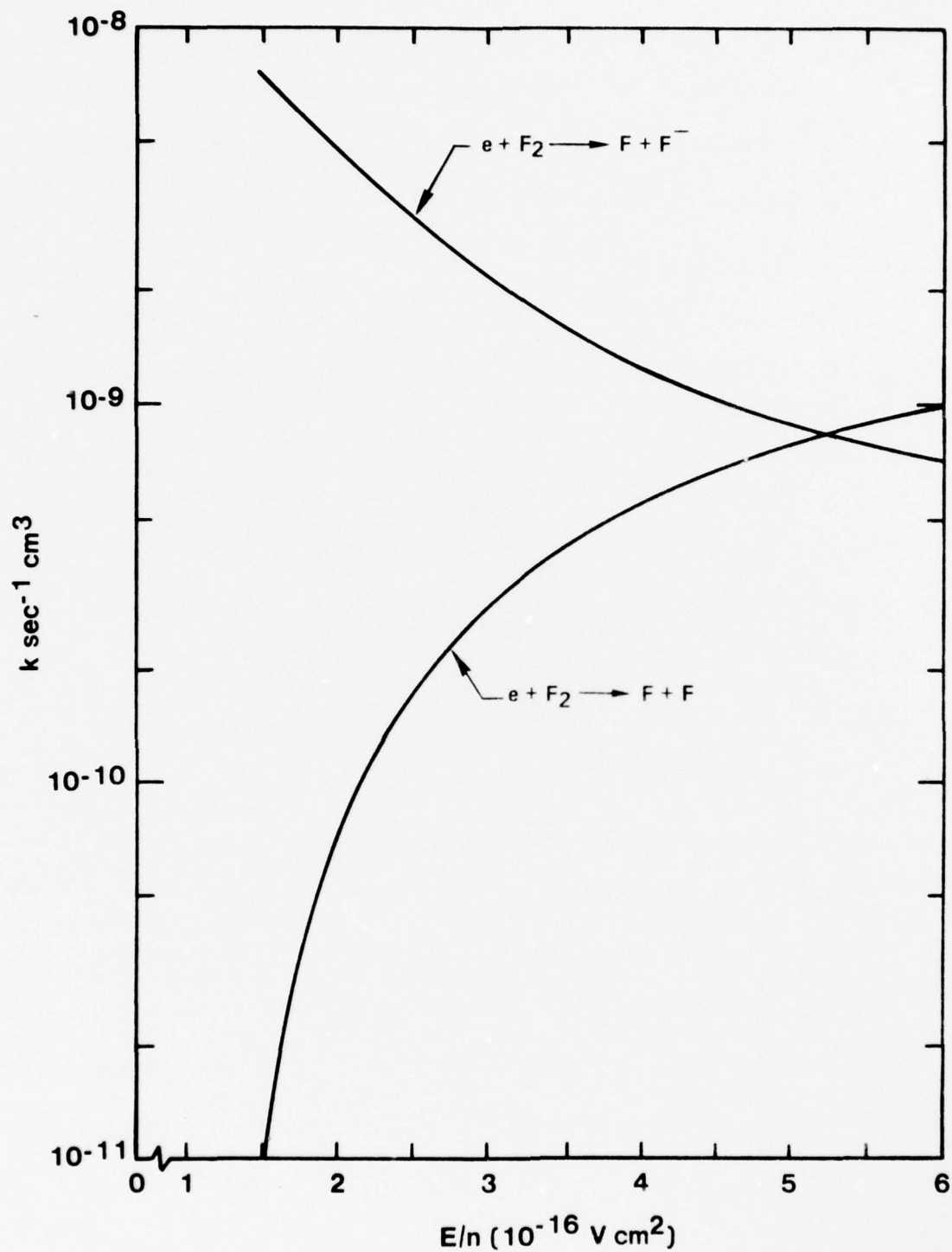
Figure 22. Computed rate coefficients for F atom production by way of dissociative attachment and direct electron impact. These approximate rate coefficients were determined using the provisional e-F_2 cross-section set discussed in the text.

77—06—84—5

52

Presented in Fig. 22 are representative rate coefficients, computed on this basis for dissociative attachment and direct dissociation. The dissociative attachment coefficient was determined using the cross-section of Fig. 17, and the direct dissociation coefficient shown in the figure is derived from a trial cross-section which rises from zero at 3.35 eV to a peak value of 2×10^{-17} cm^2 in the 4 to 6 eV range, and then decreases rapidly to a value well below 10^{-17} cm^2 above 9 eV. In the work of Ref. 10, F atom production above that produced by pure e-beam excitation (assumed to be due to dissociative attachment alone) was first observed in essentially pure F_2 for an E/n value of approximately 2×10^{-16} Vcm^2 ("T_e" $\sim$ 0.6 eV). Examination of Fig. 22 shows that for E/n $\sim 2 \times 10^{-16}$ Vcm^2 the computed rate coefficient for direct dissociation is 1 to 2% as large as the dissociative attachment coefficient, so that the contribution of direct dissociation should be observable at this E/n value. Increases in E/n showed experimental evidence of increasing F atom production, reaching a maximum of about twice that due to pure e-beam excitation for an E/n value of about 6×10^{-16}V-cm^2. Note that the data in Fig. 22 show that the contribution to F atom production from direct dissociation and dissociative attachment are indeed comparable for E/n values in the 5 to 6×10^{-16} Vcm^2 range for the provisional F_2 cross-sections used in the calculations. Thus, the experimental observations of Ref. 10 can be explained entirely on the basis of a reasonable set of e-F_2 cross-sections. Clearly, very much more data is required before it can be safely concluded that direct electronic excitation of F_2 leading to dissociation will be important for the conditions typical of rare gas-halide

Ar EX'N.

F₂ DISSOC.

ELASTIC LOSS

Kr EX'N

METASTABLE EXC'N.

F₂ VIB.

IONIZ.

1.0

0.10

0.01

0.2   0.5   1.0   2.0   5.0

E/n (10⁻¹⁶ Vcm²)

2.0   2.5   3.0   3.5   4.0

REDUCED AVE ELECTRON ENERGY
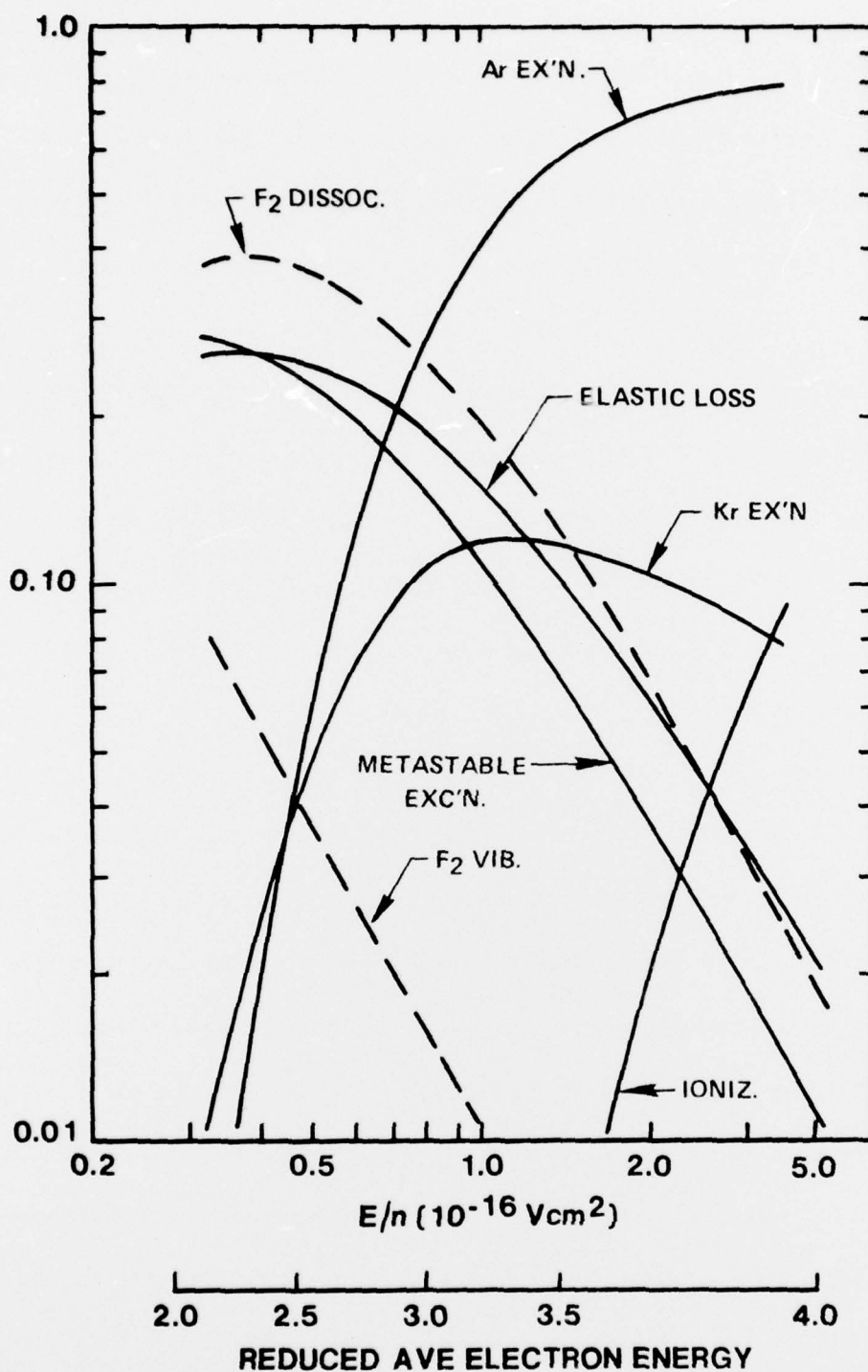
Figure 23. Computed electron fractional power transfer in an Ar-Kr-F₂ (0.95-0.05-0.005) mixture based on the provisional set of e-F₂ cross-sections discussed in the text. In these calculations the fractional ionization and fractional excitation densities were taken as constant having the representative values 1.0×10^{-6} and 1.0×10^{-5}, respectively.

77—06—84—3

54

lasers. Nonetheless, the limited experimental data available, when interpreted

in light of the provisional cross-sections discussed herein, suggest that such is

the case.

C. Effect on Discharge Kinetics

For the purpose of illustration, Fig. 23 presents the various contributions

to electron fractional power in an Ar-Kr-F_2 (0.95-0.05-0.005) mixture computed

with constant values of fractional ionization (10^{-6}) and fractional excitation (10^{-5}).

The F_2 vibrational and electronic cross-sections discussed in the previous para-

graphs were used in the calculations. These data show that energy loss to vibra-

tional excitation is likely to be relatively small in the 0.5 to 2.0 x 10^{-16} Vcm^2

E/n range of importance. However, for an electron density of about 10^{14} cm^{-3}, the

characteristic time to activate the F_2 vibrationally will be on the order of 1 μsec.

The calculations discussed in Sec. A above show that the attachment rate coefficient

may exhibit a strong dependence on the degree of F_2 vibrational excitation. Thus,

the primary influence of F_2 vibrational excitation is likely to be a change in the

attachment loss, and possibly thermal/vibrational dissociation in long pulse, high

power discharges.

By way of contrast, the electron energy loss due to F_2 dissociation excitation

may be very significant throughout the entire E/n range which is accessible. In

addition to the energy loss and implied reduction in KrF^* production efficiency,

the loss of F_2 accompanied by the production of relatively large quantities of F

atoms can impact on both the quasi-steady and stability characteristics of rare gas

halide discharges. Since the present analysis shows that such e-F_2 kinetic
effects should be expected for F_2 concentrations of a few tenths of one percent,
values consistent with experimentally determined optimums, it seems clear that
greater emphasis on such processes in the modeling of rare gas-halide discharges
is warranted.

IV. SUMMARY

During the first year of the present contract analytical models of e-beam and discharge pumped rare gas-halide laser plasmas have been developed. Major portions of this activity have been based on previously developed analytical capabilities, specifically in the areas of electron energy kinetics, molecular physics, plasma chemistry, plasma stability and low energy electron scattering theory. A particularly significant consequence of the studies completed to date has been the development of insight and understanding related to the fundamental processes dominating the production and loss of excited states. Figures 7 and 8 showing the dependence of Ar^* and KrF^* losses on pressure are particularly illustrative of the evolving understanding of basic collision phenomena in rare gas-halide plasmas.

In addition, application of resonance scattering theory has resulted in estimates of cross-sections for vibrational excitation of F_2 by electrons, which are based on a systematic evaluation of F_2 dissociation attachment data. This portion of the investigation has shown that a resonance mechanism in the $e-F_2$ system can give rise to vibrational cross-sections orders of magnitude larger than those typical of direct processes. Indeed, these results suggest that dissociative excitation of F_2 by electrons may also be enhanced by a resonance process.

Specific findings of special importance can be summarized as follows:

(1) Analysis shows that the production of KrF^* in both e-beam pumped and discharge pumped lasers can be very efficient, with overall potential laser efficiencies in the 10-20% range.

(2) Values of fractional ionization and excitation are typically in the 10^{-6}-10^{-4} range for which collisions between charged particles and charged particles and excited neutrals exert an important influence on plasma behavior.

(3) Electron-electron collisions exert an important influence on the electron distribution function and, therefore, on metastable production rates and direct ionization rates.

(4) Both direct ionization of atoms and ionization of metastables alter the characteristics of discharge pumped systems, especially their stability.

(5) Electron excitation of metastables to higher electronic levels can represent an important loss of electron energy and of metastable atoms.

(6) As total pressure is varied in the range 0.5-5.0 atm, the dominant KrF^* loss process changes from spontaneous radiation-to binary collisional quenching-to three-body collisional quenching.

(7) Application of resonance scattering theory has yielded a reasonable fit to e-F_2 dissociative attachment data over the average electron energy range 0.05-2.0 eV. The corresponding total, energy weighted vibrational cross-section has a magnitude of approximately 10^{-17} cm^2 at an average electron energy of a few eV.

(8) The characteristic time for e-F_2 vibrational excitation based on this cross-section is found to be on the order of one μsec indicating that the fraction of vibrationally excited halogen bearing molecules is likely to be large in long pulse lasers.

(9) The dissociative attachment rate for F_2 is found to exhibit a strong dependence on F_2 vibrational level.

(10) Reevaluation of available F atom production data in light of the findings of this investigation suggests that direct electron impact dissociation of F_2 may be an important loss of electron energy for typical laser conditions.

During the last half of this calendar year the analysis discussed herein will be continually refined and updated as understanding evolves and additional rate data become available. Particular future emphasis will be directed toward assessing the effect of mixture variation, e-F_2 collisions and F atom production on laser performance. It is anticipated that evolving understanding in these areas will point the way toward improving excitation techniques, laser efficiency and stability, and system lifetime.

REFERENCES

1. Digest of Summaries, 5th Conference on Chemical and Molecular Lasers, St. Louis, Missouri, April 18-20, 1977.

2. Brau, C. A. and J. J. Ewing, Appl. Phys. Lett. 27, 435 (1975).

3. Ault, E. R., R. S. Bradford and M. L. Bhaumik, Appl. Phys. Lett. 27, 413 (1975).

4. Mangano, J. A., J. H. Jacob and J. B. Dodge, Appl. Phys. Lett. 29, 426 (1976).

5. Wang, C. P., H. Mirels, D. G. Sutton, and S. N. Suchard, Appl. Phys. Lett. 28, 326 (1976).

6. Chen. H. L., R. E. Center. D. W. Trainor and W. I. Fyfe, Appl. Phys. Lett. 30, 99 (1977).

7. Biondi, M. A., "Recombination," in Principles of Laser Plasmas (G. Bekefi, Ed.), J. Wiley and Sons, New York, 1976.

8. Borst, W. L., Phys. Rev. A9, 1195 (1974).

9. DelCroix, J. L., C. M. Ferreira and A. Ricard, "Metastable Atoms and Molecules in Ionized Gases," in Principles of Laser Plasmas (G. Bekefi, Ed.), J. Wiley and Sons, New York, 1976.

10. Chen. H. L., R. E. Center, D. W. Trainor and W. I. Fyfe, J. Appl. Phys. (June 1977).

11. Lui, W. F. and D. C. Conway, J. Chem. Phys. 62, 3070 (1975).

12. McDaniel, E. W., V. Cermak, A. Dalgarno, E. E. Ferguson and L. Freidman, Ion-Molecular Reactions, Wiley-Interscience, New York, 1970.

REFERENCES (Cont'd)

13. Bohme, D. K., J. Chem. Phys. 52, 5094 (1970).

14. Nakano, H. H., R. M. Hill, D. C. Lorents, D. L. Heustis and M. V. McCusker, SRI Rept. No. MP 76-99, December 1976.

15. Velazco, J. E., J. H. Kolts and D. W. Setzer, J. Chem. Phys. 65, 3468 (1976).

16. Piper, L. G., D. W. Setser and M. A. A. Clyne, J. Chem. Phys. 63, 5018 (1975).

17. Rokni, M., J. H. Jacob, J. A. Mangano and R. Brochu, Appl. Phys. Letts. 30, 458 (1977), also Ref. 1.

18. Guzon, I. P., S. B. Kormer, L. Vvov, V. T. Punin, M. V. Sinitsyn, E. A. Stankeev, and V. D. Urlin, Sov. J. Quantum Electron. 6, 1112 (1976).

19. Helm, H., Phys. Rev. A14, 680 (1976).

20. Daugherty, J. D., J. A. Mangano and J. H. Jacob, Appl. Phys. Lett. 28, 581 (1976).

21. Champagne, L. F., J. G. Eden, N. W. Harris, N. Djeu and S. K. Searles, Appl. Phys. Lett. 30, 160 (1977).

22. Nighan, W. L., Phys. Rev. 15, 1701 (1977).

23. Birtwistle, D. T. and A. Herzenberg, J. Phys. B. 4, 53 (1971).

24. Dube, L. and A. Herzenberg, Phys. Rev. A. 11, 1314 (1975).

25. Rescigno, T. N. and C. F. Bender, J. Phys. B. 9, 1329 (1976).

26. Bardsley, J. N., A. Herzenberg, and F. Mandel, Proc. Phys. Soc. 89, 321 (1966).

27. Bardsley, J. N., J. Phys. B. 1, 349 (1968).

28. Colbourn, E. A., et. al., Can. J. Phys. 54, 1343 (1976).

29. Sides, G. D., T. O. Tiernan, and R. J. Hanrahan, J. Chem. Phys. $\underline{65}$, 1966 (1976).

30. O'Malley, T. F., Phys. Rev. $\underline{155}$, 59 (1967).

31. Hoell, J. M., et. al., J. Chem. Phys. $\underline{58}$, 2896 (1973).

32. Breig, E. L. and C. C. Lin, J. Chem. Phys. $\underline{43}$, 3839 (1965).

33. Herzenberg, A., private communication, May 1977.

34. Hay, P. J. and D. C. Cartwright, Chem. Phys. Lett. $\underline{41}$, 80 (1976).

35. DeCorpo, J. J., R. P. Steiger, J. L. Franklin and J. L. Margrave, J. Chem. Phys. $\underline{53}$, 936 (1970).

DISTRIBUTION LIST FOR ONR PHYSICS PROGRAM OFFICE
UNCLASSIFIED CONTRACTS

Director Defense Advanced Research Projects Agency Attn: Technical Library 1400 Wilson Blvd. Arlington, Virginia 22209	3 copies
Office of Naval Research Physics Program Office (Code 421) 800 North Quincy Street Arlington, Virginia 22217	3 copies
Office of Naval Research Assistant Chief for Technology (Code 200) 800 North Quincy Street Arlington, Virginia 22217	1 copy
Naval Research Laboratory Department of the Navy Attn: Technical Library Washington, D. C. 20375	3 copies
Office of the Director of Defense Research and Engineering Information Office Library Branch The Pentagon Washington, D. C. 20301	3 copies
U. S. Army Research Office Box CM, Duke Station Durham, North Carolina 27706	2 copies
Defense Documentation Center Cameron Station (TC) Alexandria, Virginia 22314	12 copies
Director, National Bureau of Standards Attn: Technical Library Washington, D. C. 20234	1 copy
Commanding Officer Office of Naval Research Branch Office 536 South Clark Street Chicago, Illinois 60605	3 copies

63

San Francisco Area Office   3 copies
Office of Naval Research
760 Market Street, Room 447
San Francisco, California 94102

Office of Naval Research   6 copies
Code 102 1P (ONR/L)
800 North Quincy Street
Arlington, Virginia 22217

Air Force Office of Scientific Research   1 copy
Department of the Air Force
Washington, D. C. 22209

Commanding Officer   3 copies
Office of Naval Research Branch Office
1030 East Green Street
Pasadena, California 91101

Commanding Officer   3 copies
Office of Naval Research Branch Office
495 Summer Street
Boston, Massachusetts 02210

Director   1 copy
U. S. Army Engineering Research
  and Development Laboratories
Attn: Technical Documents Center
Fort Belvoir, Virginia 22060

ODDR&E Advisory Group on Electron Devices   3 copies
201 Varick Street
New York, New York 10014

New York Area Office   1 copy
Office of Naval Research
715 Broadway, 5th Floor
New York, New York 10003

Air Force Weapons Laboratory   1 copy
Technical Library
Kirtland Air Force Base
Albuquerque, New Mexico 87117

Air Force Avionics Laboratory   1 copy
Air Force Systems Command
Technical Library
Wright-Patterson Air Force Base
Dayton, Ohio 45433

Lawrence Livermore Laboratory   1 copy
Attn: Dr. W. F. Krupke
University of California
P. O. Box 808
Livermore, California 94550

Harry Diamond Laboratories   1 copy
Technical Library
Connecticut Ave. at Van Ness, N. W.
Washington, D. C. 20008

Naval Air Development Center   1 copy
Attn: Technical Library
Johnsville
Warminster, Pennsylvania 18974

Naval Weapons Center   1 copy
Technical Library (Code 753)
China Lake, California 93555

Naval Training Equipment Center   1 copy
Technical Library
Orlando, Florida 32813

Naval Underwater Systems Center   1 copy
Technical Library
New London, Connecticut 06320

Commandant of the Marine Corps   1 copy
Scientific Advisor (Code RD-1)
Washington, D. C. 20380

Naval Ordnance Station   1 copy
Technical Library
Indian Head, Maryland 20640

Naval Postgraduate School   1 copy
Technical Library (Code 0212)
Monterey, California 93940

Naval Missile Center   1 copy
Technical Library (Code 5632.2)
Point Mugu, California 93010

Naval Ordnance Station   1 copy
Technical Library
Louisville, Kentucky 40214

Commanding Officer   1 copy
Ocean Research & Development Activity
National Space Technology Laboratories
Bay St. Louis, Mississippi   39520

Naval Explosive Ordnance Disposal Facility   1 copy
Technical Library
Indian Head, Maryland   20640

Naval Electronics Laboratory Center   1 copy
Technical Library
San Diego, California   92152

Naval Undersea Center   1 copy
Technical Library
San Diego, California   92132

Naval Surface Weapons Center   1 copy
Technical Library
Dahlgren, Virginia   22448

Naval Ship Research and Development Center   1 copy
Central Library (Code L42 and L43)
Bethesda, Maryland   20084

Naval Surface Weapons Center   1 copy
Technical Library
Silver Spring, Maryland   20910

Naval Avionics Facility   1 copy
Technical Library
Indianapolis, Indiana   46218